Understanding Hydrogen Variations in Silicate Glasses as a Result of Degassing: Fire-Fountaining on the Moon and Earth

A Thesis Presented for the
Master of Science
Degree
The University of Tennessee, Knoxville

Erin M. Recchuiti
May 2022

ACKNOWLEDGEMENTS

Completing this research was far from a solitary effort and I would be remiss to go without thanking those who helped me to this point. My advisor, Dr. Molly McCanta, welcomed me during the most uncertain of times and aided me in accomplishing all of this work even in light of a pandemic. My committee members Dr. Nick Dygert and Dr. Brad Thomson offered invaluable insight for the project and stepwise questions throughout the past two years. I cannot thank these three enough for their time and effort.

Dr. Eli Sklute from UMass Amherst has been instrumental in the successful acquisition of FTIR data and an impeccable guide for data processing. Dr. Darby Dyar's words of wisdom ensured each conference abstract was at its utmost best. The EMPA work would not have been possible without the patience and enthusiasm of Allan Patchen. Without Eli, Darby, and Allan the backbone of this project could not have been completed.

Thank you CJ for our weekly writing meetings, your support and input helped keep me on track and sane. Dr. Amy Fagan will always have my gratitude for being the lifelong mentor we all hope to have. Jake, your math wizardry will continue to baffle me though I am eternally grateful for it. Ivy and Morgan I could not imagine this experience without our laughs. The 7th floor office dwellers have my gratitude for being my sounding board for the past two years. Thank you to my parents for being the sounding boards outside of office hours even if you guys didn't always quite follow the science. And thank you Cameron for always cheering me on through the good and bad days.

ABSTRACT

Volatiles, particularly hydrogen, play a key role in volcanic eruptions, especially explosive eruptions like fire-fountaining [e.g., Saal et al. 2002; Dixon 1997; Arndt & von Engelhardt 1987; Yoder 1976]. Discerning volatile abundance and behavior during ascent and eruption can aid in understanding the source melt and primary volatile content of planetary interiors. Volcanic glasses are samples closest to the primary melt, as they quench quickly enough to limit fractionation or crystallization. This is paramount for volatile studies, especially pertaining to water as its constituents are oxygen and hydrogen. Hydrogen is the most volatile element and one of the first to vacate the system via degassing, therefore glasses quenched within minutes can preserve traces of water [Ustunisik et al. 2015; Saal et al. 2008]. There are several instances of terrestrial fire-fountain eruption styles such as Hawaiian glass beads. The products of these fire-fountain events are glass beads have been likened to the glass beads returned by the Apollo missions. The picritic glasses from Apollo 15 and 17 samples have been evaluated to determine the amount of volatiles lost during degassing during ascent and subsequent eruption [Hauri et al. 2015; Saal et al. 2008]. High-resolution measurements of water in lunar glasses are needed to constrain lunar volatile evolution.

This work evaluates the abundance and distribution of water in glass beads from the Kilauea volcanic complex of Hawaii as well as lunar glass beads from Apollo 15 and 17 via FTIR analyses. The lunar glasses are from samples 15427,83 and 74220,226 as well as fresh beads from the Apollo Next Generation Sample Analysis (ANGSA) program core 73002. Results of this work indicate that degassing is most effective via fractures and vesicles, though core-to-rim degassing is also present in larger samples. The findings that the ANGSA Apollo 17 samples have lower water abundance than 15427,83 suggests that samples with modification from previous analyses can impact the accuracy of the data. These data indicate that degassing via fractures and vesicles disrupts

preservation of diffusive core-to-rim degassing and that the smaller lunar glasses can show hydration distributions that suggest complete degassing and some in-gassing.

TABLE OF CONTENTS

LIST OF TABLES

LIST OF FIGURES

SECTION 1. INTRODUCTION

Explosive volcanic eruptions are observed on the Earth today, while both recent and ancient eruptive materials have been identified on Earth as well as the Moon, Mars, and Mercury [e.g., Broz et al. 2021; Weider et al. 2016; Swanson et al. 2014; Thomas et al. 2014; Elkins-Tanton 2003]. In the context of the Earth and Moon, the timeline for active volcanic periods spans billions of years (Figure 1). Volatile exsolution is the primary driver of explosive eruptions [Arndt & von Engelhardt 1987; Yoder 1976], products of explosive eruptions serve as the primary record of the volatile composition of planetary interiors. Therefore, quantifying volatile concentrations can provide important constraints on the primary volatile content of a planetary body and its subsequent evolution. Studying volatile element composition, speciation, and abundance during volcanic events is also crucial for understanding influence of volatiles on mantle melting, magma crystallization and eruption dynamics, as well as spatial distribution that can provide information on mantle conductivity, mantle heterogeneity, and crustal recycling [Hauri 2002; Saal et al 2002; Simons et al. 2002; Jung & Karato 2001; Gaetani & Grove 1998; Hirth & Kohlstedt 1996; Kingsley & Schilling 1995; Zhang & Zindler 1993; Javoy et al. 1982].

In the early solar system, extreme cold temperatures permitted H_2O to condense in areas outside the snow line (~1-5 astronomical units (AU), where 1 AU is Earth distance from the sun) [Saal et al. 2008]. The dichotomy of water-enriched and water-depleted areas of the solar system can be observed most plainly by the large gaseous outer planets (Jupiter, Saturn, Uranus, and Neptune) and the rocky inner planets (Mercury, Venus, Earth, and Mars) respectively [Morbidelli et al. 2010]. H_2O (water) vapor is the most easily liberated gas from melts and is also one of the first volatiles to degas at low pressures (< 50 kbar), fully degassing within 10 minutes in erupted materials [Ustunisik et al 2015; Weston et al. 2013; Moore 1970]. H_2 is the most abundant species of hydrogen and can be a product of H_2O degassing. H_2 has a low solubility in magmas and

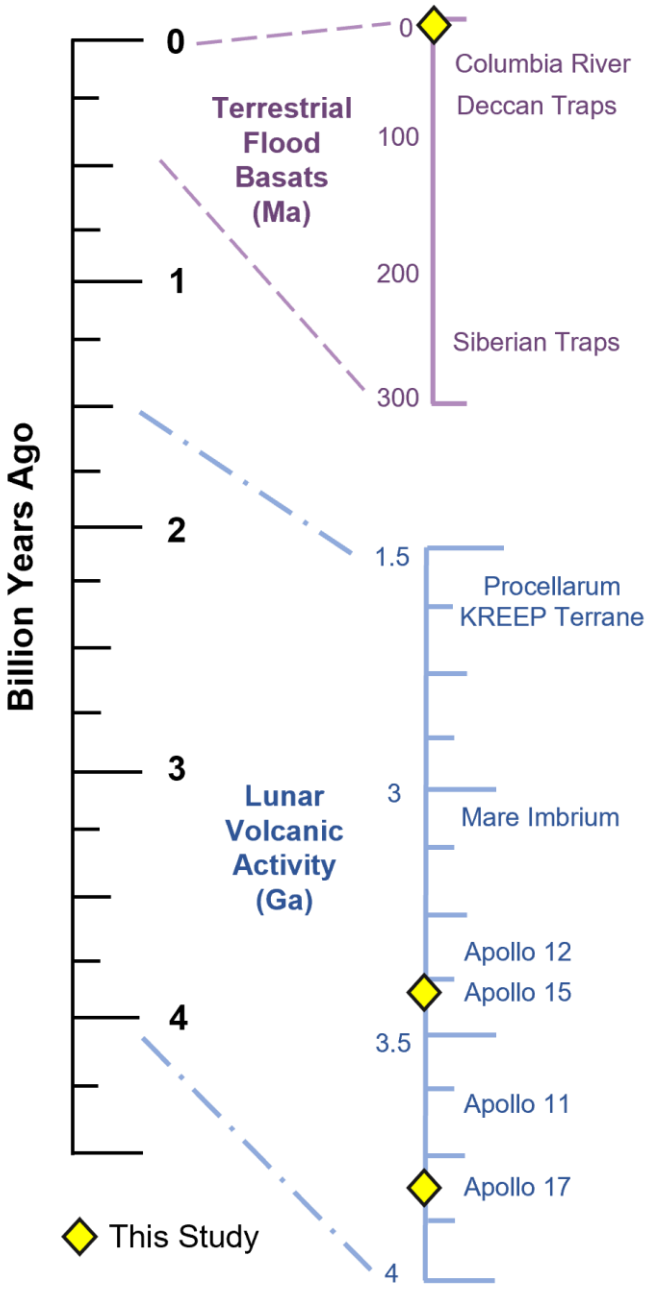

Figure 1. Timeline indicating the relative ages of some well-known terrestrial flood basalts and lunar eruptions and Apollo samples modified from Head [1976]. The yellow diamonds indicate the samples in this work including the lunar Apollo 15 and 17 glasses and terrestrial EPR pillow basalts and Hawaiian glasses.

rapid diffusivity that can have the effect of samples appearing “dry” as a result of 98% of H_2 being lost during degassing of a crystalline sample [Renggli et al. 2017; Sharp et al. 2013; Saal et al. 2008]. Therefore, to quantify melt H_2O or H_2 it is important to utilize a glassy sample which implies quenching within 2-5 minutes of eruption thereby allowing for reduced opportunity for total degassing [Hauri et al. 2015; Wetzel et al. 2015; Saal et al. 2008]. Previous studies suggest there may be as much as 260-745 ppm H_2O in lunar glasses, similar to that of terrestrial mantle, 50–270 ppm [Gose et al. 2009], although all analyzed lunar samples have been nearly completely degassed [e.g., Saal et al. 2008, Saal et al. 2002]. Understanding hydrogen degassing may be a means of defining the differences of H_2O content and oxygen fugacity (fO_2) within lunar samples [Sharp et al. 2013].

Here I present new data to constrain the concentration of H_2O in terrestrial and lunar glass samples and use the data to evaluate melt degassing behavior. The samples in this study include those of the ANGSA core 73002 which have been recently opened and have no prior research. Correlations between H abundance and magmatic fO_2 are investigated to determine how H loss affects the oxidation state of the melt. Understanding the oxidation state of the mantle will aid in illuminating the partitioning of elements and water between the melt and mineral phases for the Moon. This project will further investigate the relationship between degassing of H_2, the relationship between H_2O and oxidation state, and the degassing behavior of hydrogen during ascent and eruption in terrestrial pillow basalts to ascertain the potential application to lunar context. The primary hypothesis of this study that will be tested is that fractures formed in the larger glasses during cooling allow for hydrogen to exit solution more readily and therefore is the preferred method of degassing whereas the small glasses devoid of fractures exhibit core-to-rim degassing. Examples of support for preferential degassing via fractures are significant depletion or abundance of hydrogen near fractures. The depletion would represent successful degassing and abundance would indicate incomplete degassing due to complete

cooling of the bead or partial fractures. Additional hypotheses are that there will be (a) general core to rim degassing regardless of size and (b) degassing of hydrogen via vesicles in the glasses.

SECTION 2. BACKGROUND

Explosive Volcanism and Silicate Glasses

Fire-fountain eruptions are a type of explosive volcanism that sprays blebs or melt droplets from volcanic vents that can result in tall fountains of lava spraying onto the surface [Parfitt & Wilson 1995; Head 1976; Macdonald 1872] (Figure 2). These high-energy eruptions result in volcanic products similar to the original composition of the parent melt due to the rapid eruption and cooling of the lava which are factors that limit crystallization and fractionation [e.g., Schmincke 2004; BVSP 1981]. The rapid cooling rater results in quenching that limits the amount of volatiles that are typically completely degassed from a crystalline igneous rock [Peng et al. 2019; Hauri et al. 2011, 2015; Shearer et al. 1991]. Therefore, volcanic glasses produced via fire fountain eruptions are ideal for volatile studies as they have a high likelihood of being geochemically similar to the melt and recording volatile content even after ascent and eruption [e.g., Saal et al. 2008].

Hawaii frequently exhibits fire-fountaining eruptions and the glass beads found in places like the Kilauea volcano deposits have been likened to glass beads collected by the astronauts on the Apollo missions from the lunar regolith [Parfitt & Wilson 1995; Head 1976; Macdonald 1972]. The lunar regolith contains an abundance of volcanic glasses with varying textures and compositions that are believed to have been produced via fire-fountain type eruptions [Parfitt & Wilson 1995; Delano 1986; Head 1976; Macdonald 1972]. Investigating the origin of lunar glass beads is enhanced by utilizing analogue terrestrial samples like the glass beads from Hawaiian eruptions [Wilson & Head 2017; Taylor 1982; BVSP 1981; Wilson & Head 1981; Guest & Murray 1976; Head 1976; Schultz 1976]. From these studies we can deduce similarities and or differences between melt geochemistry and volatile content on the Earth and Moon as well as how eruption styles may differ.

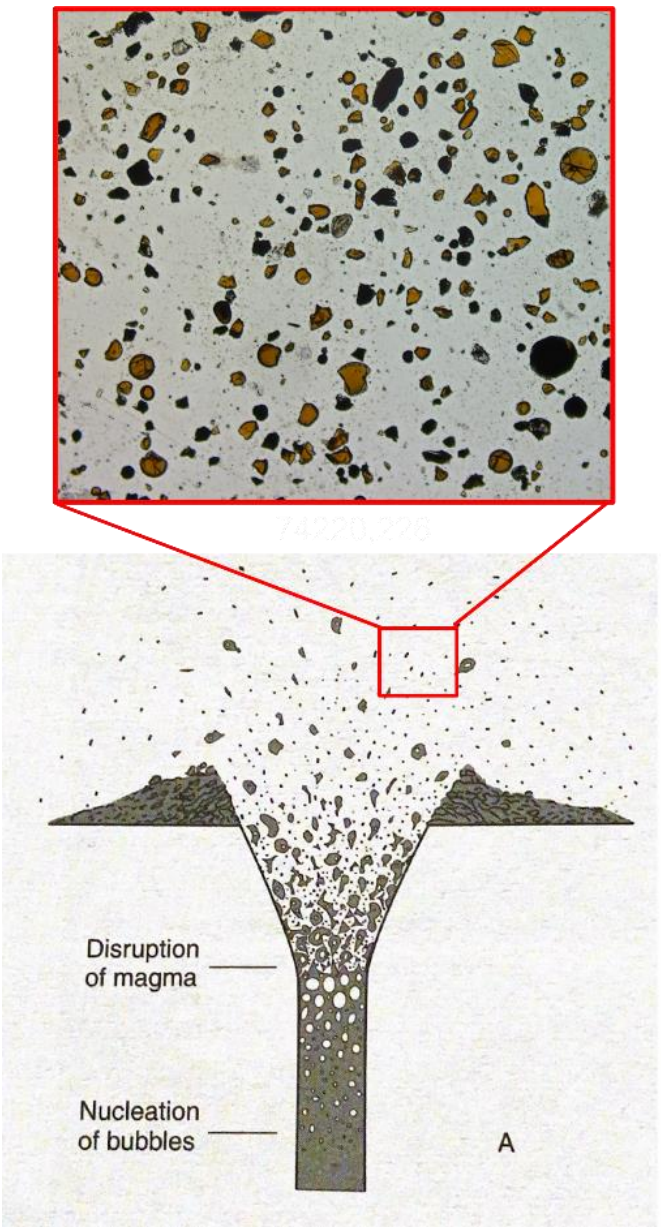

Figure 2. Cross section from Philpotts & Ague [2009] indicating the nucleation point of vesicles and the disruption of magma resulting in fragmentation of the melt with the glass products being deposited in the surrounding area. The subset image is of sample 74220,226 with orange glass beads and shards present in a plain polarized light image.

Terrestrial Explosive Volcanism

There are distinct differences between the volcanic glass beads that have been collected and studied on Earth versus those obtained via the Apollo program. The Hawaiian glass beads that have been studied are vesicular and generally larger than the picritic beads from the Apollo samples (mm vs μm, respectively) [e.g., Rutherford & Papale 2009]. The presence of vesicles in terrestrial samples is related to the greater volatile abundances present within Earth versus the Moon. Nonetheless the glass beads can still be used to constrain potential lunar eruptive volatile loss mechanisms. This work will further our understanding of the abundance and amount of H lost during degassing while a melt ascends the conduit to erupt via fire fountaining, allowing for more insight into magmatic volatile loss processes.

Pele's Hairs and Tears

When magma erupts, it is partially or completely fragmented by processes like gas expansion via exsolved gases, steam resulting from interactions with the hydrosphere, or air entrapped in the melt [e.g., Elkins-Tanton 2003; Zimanowski et al. 1997; Parfitt & Wilson 1995]. In subaerial explosive eruptions of low viscosity basaltic melts, such as Hawaiian fire-fountaining, pyroclastic products of almost pure glass are produced called Pele's hairs (rods) and Pele's tears (beads) [Cannata et al. 2019; Heiken & Wolhetz 1985]. Hawaiian eruptions have a variable ascent rate that can be greatly affected by bubble formation and coalescing during degassing, and the resultant changes in the viscosity of the melt that can result in large glass blebs or smaller droplets being produced by the fire-fountaining [Parfitt & Wilson 1995]. The "spray" of glass droplets and beads produced by Hawaiian fire-fountaining are structurally similar to lunar pyroclastic deposits from which lunar glass beads have been collected by the Apollo missions and therefore the association of a similar formation mechanism has been inferred [Wilson & Head 2017; Guest & Murray 1976; Head 1976]. Early ideas around the abundance and production of Pele's tears centered on

similarities of the spherical glass objects observed in meteorites [Sorby 1877]. It is known today that the spherules in meteorites have no connection to the glass beads produced from fire-fountaining [e.g., McSween 1999; Heide & Wlotzka 1994]. Hawaiian Pele's hairs and tears are products of supercooled basaltic magma that are ejected in high velocity spurts [Zimanowski et al. 1997; Shimozuru 1994; Katsura 1967]. The velocity is the main factor controlling whether a tear maintains sphericity or elongates to a hair [Cannata et al. 2019; Shimozuru 1994]. Low spurting velocity is associated with spherical Pele's tears and high spurting velocity is associated with long thin Pele's hairs [Shimozuru 1994]. Equation 1 is used to calculate Pele's number (Pe) where a small Pe is related to tears and large Pe values is related to hairs [Shimozuru 1994].

$$Pe = \frac{\rho v \eta}{\rho_o \sigma}$$

Equation 1. Pele's number (Pe) is the density of the liquid (ρ) times velocity (v) and viscosity (η) divided by density of the rock (ρ_o) times surface tension of the liquid (σ).

There have been many experimental [e.g., Zimanowski et al. 1997; Shimozuru 1994; Katsura 1967] and empirical [e.g., Cannata et al. 2019; Moune et al. 2007; Phillips 1894; Dana 1879 Phillips 1894] studies centered on uncovering the unique morphology and chemistry of Pele's hairs and tears. The consensus on the formation of Pele's tears and hairs is that a tear is the principal form from which a hair can develop (Figure 3). Evidence for the two-step process can be seen in the elongated vesicles observed in Pele's hairs that can span the entire length of the hair and tumor-like structures on the hairs in which microlites (most often plagioclase and or olivine) prohibit stretching [Cannata et al. 2019; Moune et al. 2007]. Chemical zoning has been noted in both hairs and tears to indicate variation from core to rim as well as fracture distinction [Moune et al. 2007].

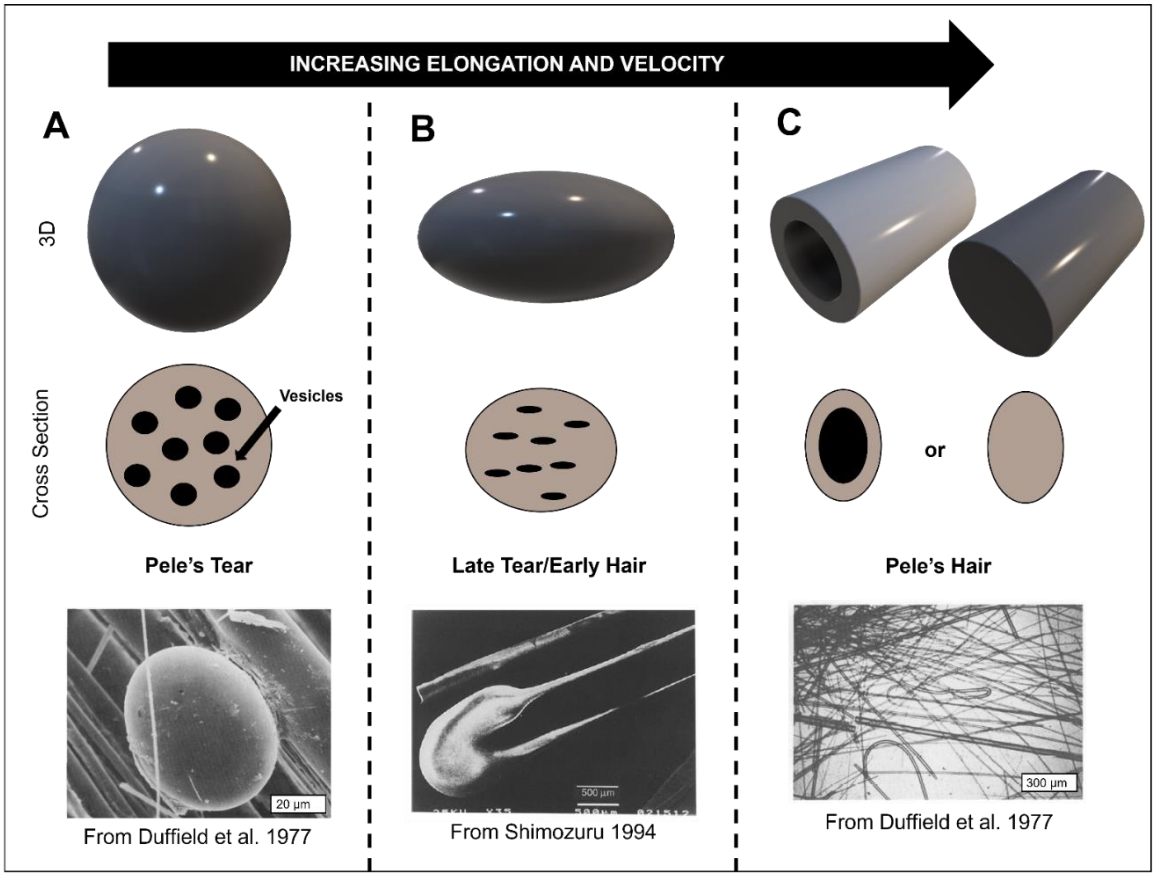

Figure 3. Schematic indicating the formation of a Pele's hair from a Pele's tear via elongation of the tear that can result in a hair with one massive vesicle or void of vesiculation. Images of a tear (A) from Duffield et al. [1977], a late tear or early hair (B) from Shimozuru [1994], and a hair (C) from Duffield et al. [1977] are examples of the progression from a tear to a hair.

Lunar Explosive Volcanism

Glasses

The prior hypothesis that the Moon was depleted in volatiles and anhydrous has been disproven [Zhang et al. 2019; Hauri et al. 2015 & references within; Saal et al. 2008]. Saal et al. [2008] quantified volatiles within lunar glass beads from Apollo 15 and 17 samples (ranging in size from 100-400 μm) via secondary ion mass spectrometry (SIMS) analyses (Figure 4). The range in size allowed for investigations into the role of major and trace elements on volatile variation within the beads to determine if degassing eliminated original volatile content [Saal et al. 2008]. Saal et al. [2008] found that there was preservation of the original volatile content even with substantial degassing.

To reach their findings, Saal et al. [2008] utilized two methods, analytical techniques and modelling. These analytical techniques included individually analyzing glass beads for major and trace elements with electron microprobe and NanoSIMS instruments. With their data, Saal et al. [2008] then modeled cooling rates with input parameters of sphere radius, temperature of the melt during eruption, the cooling rate for the bead, the initial volatile concentration, diffusion coefficient of volatiles, and the rate of evaporation at the surface of the melt sphere. The samples included in their findings are very low-Ti (15427,41), low-Ti (15427,41), and high-Ti glasses (74220,864).

The utilization of glasses with variable composition accounts for variability in initial volatile content based on major melt composition [Saal et al. 2008]. This is particularly evident in the very low-Ti glass beads which returned a radial concentration profile with the volatiles decreasing from core to rim. For example, water content in the very low-Ti bead ranged from 30 ppm in the core to 14 ppm at the rim. Saal et al. [2008] used data like the very low-Ti bead in their models and they deduced that cooling rates between 2 and 3 Ks^{-1} are the best fit over a time of 2 to 5 minutes for quenching to produce the degassing observed in the lunar samples. Their calculated initial water content for the lunar initial melt is 745

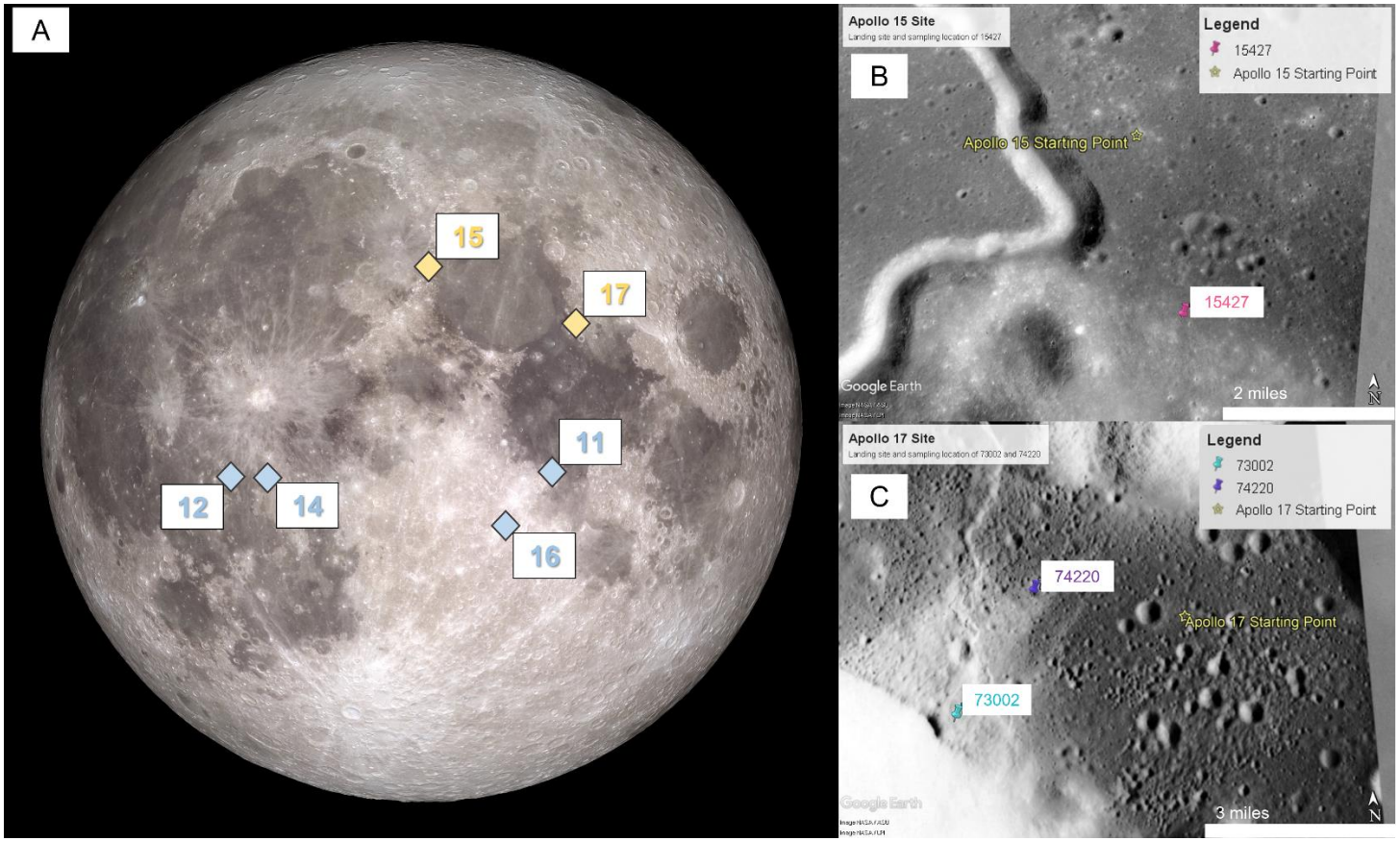

Figure 4. (A) Approximate location of landing sites from the Apollo program's 11, 12, 14, 15, 16, and 17 missions. (B) Landing site for Apollo 15 and sample collection location for 15427. (C) Landing site for Apollo 17 and the sample collection locations for 74220 and 73002 [modified from https://moon.nasa.gov/system/resources/detail_files/77_lro_fullmoon.jpg]. On the right are the sampling locations for samples 74220, 73002, and 15427 plotted on using Google Earth Pro [Ryder 1985; Wolfe et al. 1981].

ppm with a minimum requirement of 260 ppm to produce degassing observed in their samples. 745 ppm is vastly more hydrous than previous estimates for the Moon and opened the door to future studies exploring the history of the Earth-Moon system and volcanism on the Moon. The results of subsequent and ongoing studies regarding lunar volatiles can aid in the understanding of the lunar water budget, the geochemistry of the lunar mantle, and the formation and evolution of the Moon.

Explosive lunar volcanism is thought to be driven by the exsolution and expansion of CO_2 and H_2O gases [Rutherford & Papale 2009]. As lunar samples are relatively rare, terrestrial analogues are often analyzed due to their compositional similarity which can provide insight to underlying physical processes related to eruption and volatile degassing (Table 1). Hawaiian glass beads and mid-ocean ridge pillow basalts are useful terrestrial analogues as they both are products of basaltic volcanism with quenched glasses, which preserve the amount of volatile degassing experienced during magma ascent. Hawaiian glass beads and rods are particularly valuable as analogue samples since they are formed by explosive fire-fountain-style eruptions, similar to how the lunar glass beads are inferred to have formed [Wasson et al. 1976].

Apollo Next Generation Sample Analysis and Space Weathering

The Apollo missions returned a plethora of samples from the lunar surface and recognized that the technology of the mid-20th century would advance in the coming decades with the ability to return optimal science [Anand et al. 2014]. With the foresight to sequester samples (i.e., Apollo Next Generation Sample Analysis) until technology and analytical techniques had advanced to the point of returning the most accurate data, there is now an opportunity to gain previously unobtainable information about the lunar interior.

Space weathering is a process that occurs on airless planetary bodies that lack a magnetic field in which micrometeorites bombard the surface and solar

Table 1. Compositional major and minor oxides from electron microprobe data of lunar glass beads [McCanta et al. 2017], Hawaiian picrite basalts from Kilauea [Macdonald 1949], and mid-ocean ridge basalts (MORBs) [Lanzirotti et al. 2008].

Sample Type	SiO_2	TiO_2	Al_2O_3	Fe_2O_3	FeO	MnO	MgO	CaO	Na_2O	K_2O	P_2O_5	Cr_2O_3	H_2O	Total
Moon	40.16	12.58	7.82	--	20.38	0.33	5.19	12.01	0.32	0.05	--	0.37	--	99.21
Hawaii	47.25	1.61	9.07	1.45	10.41	0.13	19.96	7.88	1.38	0.35	0.21	--	0.12	99.82
MORB	49.7	2.6	12.0	--	12.7	0.2	9.6	10.2	1.9	0.5	0.2	--	--	99.6

winds implant H-ions and high energy photons [Wu et al. 2019; Hapke 2001; Denevi et al. 2014; Igami et al. 2021]. The Moon lacks an atmosphere and stable magnetic field and is therefore a strong candidate for substantial space weathering to occur. Spaces weathered surfaces typically contain optically dark, reddened, low albedo surface materials with variable particle size [Igami et al. 2021; Hapke 2001]. These attributes are only surficial as indicated by cores returned from the Apollo missions in which the space weathered material lightens in color after the first tens of millimeters and eventually transitions to near pristine, but still weathered, regolith (Figure 4). When describing the gradient from highly weathered to more pristine, there is a maturity index that utilizes nano-phase iron to quantitatively classify the state of the regolith [Matsumoto et al. 2021; Wu et al. 2019]. The different categories for regolith maturity are mature, submature, and immature [Wiesli et al. 2003]. The samples within this work only propagate to the submature depth of regolith maturity. The Moon is unique in its experience with space weathering due to its tidal lock with the Earth. This relationship results in varied degrees of weathering based on proton precipitation rates on the nearside of the Moon versus the farside [Kallio et al. 2019]. This is important to be cognizant of given the current sample bias in the Apollo mission returned samples from only the nearside.

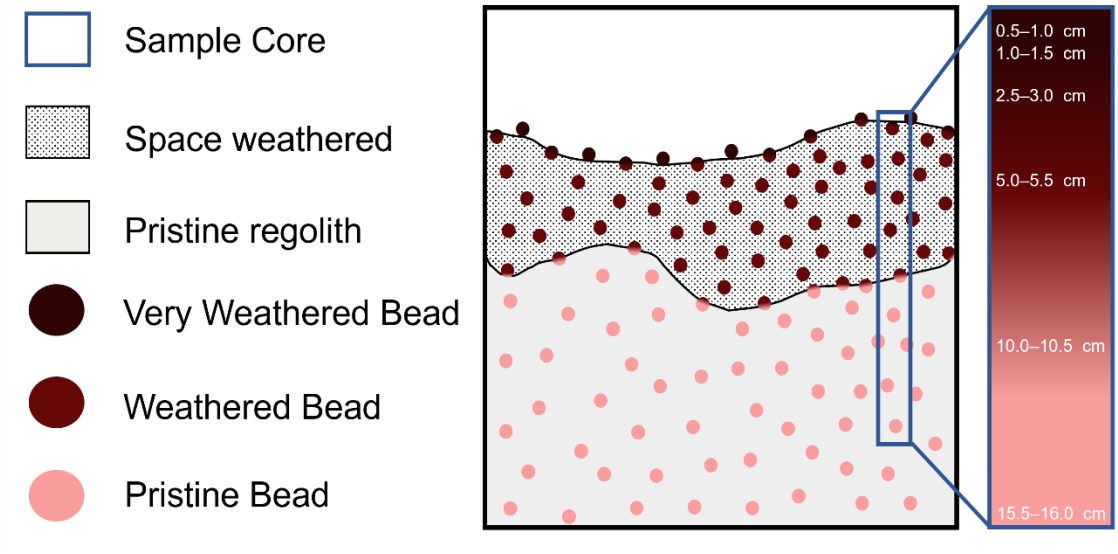

Figure 5. Cross section of lunar regolith with the upper portion modified by space weathering underlain by pristine unmodified regolith. The circles represent glasses that have been very space weathered (maroon), weathered (red), and not weathered (salmon). The gradient beads represent those in intermediate areas between very weathered and weathered regolith or weathered and more pristine regolith. The navy rectangle is an example of the contents of regolith cores with the sampling intervals for core 73002. Sample locations are as follows: 73002,344 from 0.5–1.0 cm, 73002,347 from 1.0–1.5 cm, 73002,350 from 2.5–3.0 cm, 73002,353 from 5.0–5.5 cm, 73002,355 from 10.0–10.5 cm, and 73002,357 from 15.5–16.0 cm depth range.

SECTION 3. METHODS

Sample Preparation

The samples analyzed include both terrestrial and lunar volcanic glasses. The terrestrial samples consist of Hawaiian glass beads (Pele's tears), strands of Pele's hair from Hawaii (glass rods), and an East Pacific Rise (EPR) mid-ocean ridge (MOR) pillow basalt. The lunar samples studied are glass beads from Apollo 17 (sample 74220,226), Apollo 15 (15427,83) and the Apollo Next Generation Sample Analysis (ANGSA) program core 73002. Core 73002 was collected on the Apollo 17 mission with a double drive tube containing light mantle material near the Lee Lincoln Scarp (Figure 4C) [Wolfe et al. 1981]. 73002 was 22 cm long and sampled in the same core as sample 73001 with a total length of 56.9 cm [Wolfe et al. 1981]. The 74220,226 sample is a thin section that contains a multitude of orange glass beads and shards with varying degrees of fracture and has been in circulation of various projects for several years (Figure 7). 15427,83 is a regolith breccia with glass beads and shards along with other lithic clasts in entrained within a matrix. The ANGSA glass beads allow for analysis of pristine samples that have not undergone any prior destructive forms of geochemical analysis and therefore are expected to provide data that is representative of the glass with little to no contamination. Additionally, beads have been sampled from increasing depth downcore.

The Hawaiian glass beads were set in a silicon mold and then cut using a precision wire saw with an abrasive slurry at the University of Tennessee Knoxville. The EPR pillow basalt was set in epoxy and cut as a thick section at the University of Massachusetts, Amherst. The Apollo samples 74220,226 and 15427,83 were already prepared as thin sections with the samples set in epoxy prior to this work. The Pele's hairs and tears were set in 1-inch epoxy rounds and polished as a thick section. The tears were set in the round to allow for the polishing to reveal a cross section of the width of the hair. The ANGSA samples were from core 73002 and include beads and shards from throughout the space

weathering profile. The 73002 samples were individually set into epoxy drops to allow for easier handling when putting individual beads into 1-inch epoxy rounds. Once the ANGSA beads were in the 1-inch round, the samples were then hand polished to mitigate the risk of sample loss with an automated polishing sequence.

Fourier Transform Infrared Spectroscopy

Results for the Pele's tears and hairs, EPR pillow basalt, and all lunar samples (74220,226, 15427,83, and ANGSA core 73002) were acquired by the following methodology. Fourier transform infrared (FTIR) reflectance spectroscopy analyses were collected using both (1) a Bruker Vertex 70 with a Hyperion 3000 microscope with a mercury cadmium telluride (MCT) point detector and a 64×64 focal plane array (FPA) detector at the University of Massachusetts, Amherst, and (2) the Bruker Lumos II equipped with 64×64 pixel FPA detector at Bruker Demo Laboratory in Billerica, MA. The spectral range was 4000 to 800 cm^{-1}. The samples were lightly polished prior to analysis to remove surface H_2O that could contaminate the results. FPA image acquisition was guided by coarse MCT maps that were at a higher spectral (4 cm^{-1}) and lower spatial resolution. The spectra that were obtained was then offset-normalized to the baseline value 4000-3990 cm^{-1}.

Noisy pixels were removed manually in each image prior to binning. The signal to noise ratio (SNR) was increased for the maps by binning. 2×2, 4×4, and 8×8 bins were examined to find the best spatial resolution with adequate SNR. In some cases the SNR was adequate enough to not require binning at all. The hydrogen maps were made applying a peak area integration (OPUS B class integration) of the broad hydration feature from approximately 3660-2996 cm^{-1} (Figure 6). This feature has been shown to be due to the OH in mineral structures and has been correlated to hydrogen concentrations [Bell & Rossman 1992; Johnson & Rossman 2003; Seaman et al. 2006]. The epoxy-associated feature (as a result of the sample being slide-mounted) that appears at 2990 cm^{-1} required that endpoints of integration be manually chosen with the additional

benefit of averaging out thin-sample sinusoidal interference (Figure 7). The current maps provide the ability to qualitatively assess the hydrogen distribution across the sample. Analyses for the Hawaiian glass beads are continuing.

Water abundance calculations were preformed following Stopler [1982] and using the Beer-Lambert Law (Equation 2). The density values for the samples in this study are unknown therefore the density of previous experimental work that produced glass beads compositionally similar to our samples were used [Zhang et al. 2019; Zhang et al. 2017; Vander Kaaden et al. 2015; Parker et al. 2011]. The molar absorptivity value was based on the findings of Ohlhorst et al. [2001] concerning basaltic glasses. Thicknesses of the samples were verified utilizing the methods of von Aulock et al. [2014] (Equation 3). The absorbance was found by integrating the area of expected hydration (3660 to 2996 cm^{-1}) of the spectra in OPUS that includes both OH and molecular H_2O vibrations since the glasses are not saturated to the point of using species specific vibrations (i.e., 3500 to 3200 cm^{-1}) [Zhang et al. 2019; McIntosh et al. 2017; Zhang et al. 2017; Pearson et al. 2014; Mandeville et al. 2002; Dixon et al. 1995].

$$c = \frac{18.02 \times Absorbance}{d \times \rho} \times \frac{1}{\varepsilon}$$

Equation 2. Beer-Lambert law with *c* as the H_2O concentration as weight fraction, 18.02 is the molecular weight of water, Absorbance is the height of the absorption peak, *d* is the thickness of the sample in cm, ε is the molar absorptivity in liters/mol-cm, and ρ is density of the sample in g/liters.

$$d = \frac{m}{2n\,(v1 - v2)}$$

Equation 3.Thickness calculation where *d* is the sample thickness in cm, *m* is the number of waves in a selected wavenumber range, *n* is the refractive index, and *v*1 and *v*2 are the highest and lowest wavenumbers respectively in cm^{-1} in the selected interval.

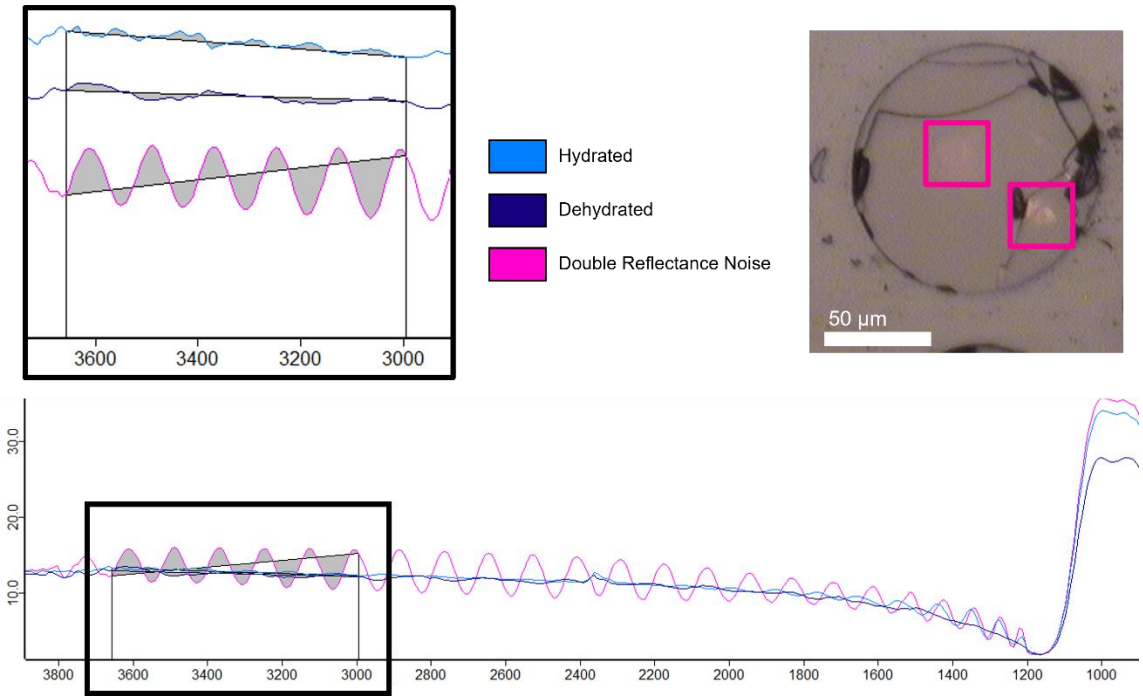

Figure 6. Examples of spectra within the hydration feature range used in this work with the blue spectra indicating a strong hydration, purple as poorly hydrated or dehydrated, and the pink as double reflectance interference. The top right reflected image of 74220,226 bead 4 shows in the pink boxes that double reflectance can often be optically observed.

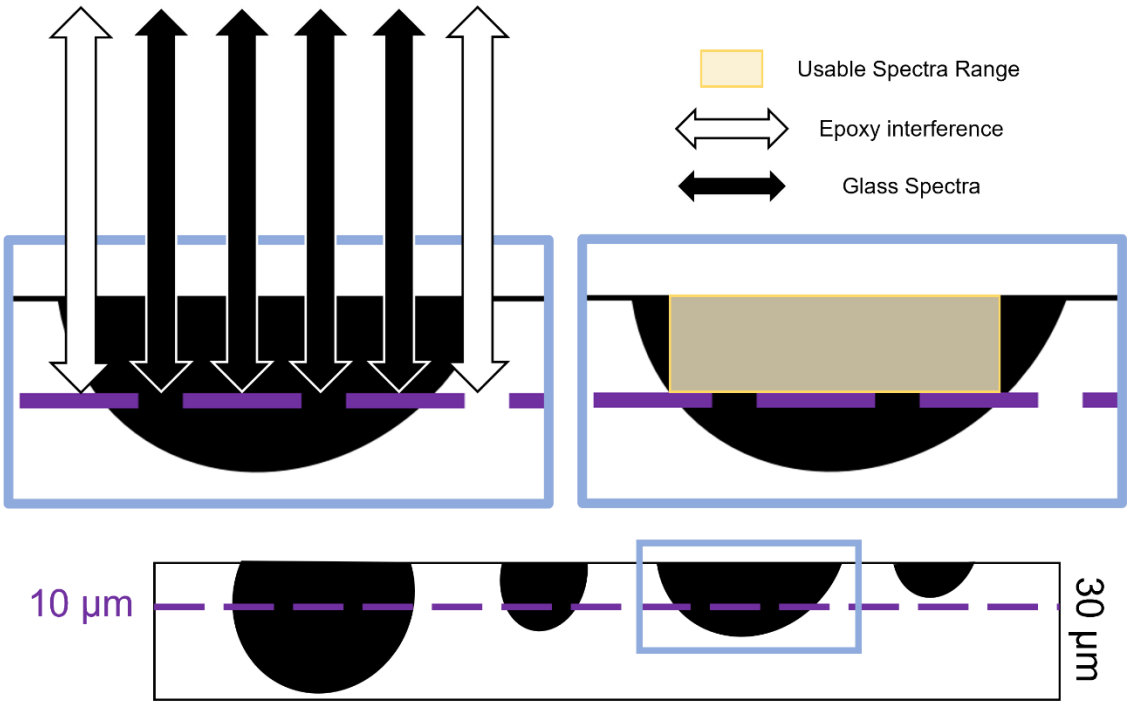

Figure 7. Bottom cartoon of beads in a 30 µm thin section with the maximum permeation depth of the reflected beam shown at 10 µm, the bead furthest right is too thin and does not pass the permeation depth. Top left indicates areas where the reflected area is returning data for the epoxy (white arrows) or glass bead (black arrows) for the medium sized bead outlined in blue in the bottom image. Top right indicates the area of the bead returning glass spectra (yellow shaded box) is not to the full edge of the bead, as the rims are too thin to return no epoxy interference.

Electron Microprobe Analyses

Electron microprobe analyses were conducted at the University of Tennessee with a Cameca SX-100 electron probe and 15 kV acceleration voltage. Samples were carbon coated and a 10 μm spot size was used. A sodium loss routine was run for glass analysis [Neilsen & Sigurdsson 1981]. Peak count times were run for 20 seconds for Na, SI, Al, and K, 30 seconds for Mg, Ca, and Ti, 40 seconds for P, Fe, Mn, and Cr, and 50 seconds for S. These count times resulted in a detection limit of approximately 300 ppm (0.03 wt%) therefore any element found to be less than 0.03 wt% was listed as >0.03. A minimum of four points were collected per sample, though in some cases more were collected in the case of larger samples and those containing crystalline phases as well as glass. Compositional data were obtained using natural and synthetic basalt glass standards from C.M Taylor Corporation with diopside (Si, Ca), albite (Na), synthetic spinel (Al), orthoclase (K), hematite (Fe), rutile (Ti), spessartine (Mn), olivine (Mg), chromium metal (Cr), fluorapatite (P), and sphalerite (S).

X-Ray Absorption Spectroscopy

X-ray absorption near edge spectroscopy (XANES) analyses of the EPR pillow basalt were collected in situ at the GSECARS X-Ray Microprobe (13-ID-E) at Advanced Photon Source at Argonne National lab [Lanzirotti et al. 2018]. The methods for analyses can be found in Lanzirotti et al. [2018].

SECTION 4. RESULTS

East Pacific Rise Pillow Basalt

Mid-ocean ridge basalts are excellent examples of an explosive volcanic product that formed under high pressure conditions that prevent complete volatile degassing, as the pressure at the base of the ocean water column is higher than a subaerial eruption [Weston et al. 2013; Saal et al. 2002]. MORBs are additionally intriguing with the proposed multistage degassing that occurs as the melt moves from the magma chamber, ascends, and quenches after eruption [Weston et al 2013; Paotina & Martelli 2007]. Decompression is the primary driving force of volatile loss during ascent. When erupted into water, the melt quenches over the course of minutes to hours to form the glassy rind of the pillow basalts [Weston et al. 2013; Paotina & Martelli 2007] (Figure 8).

Samples of mid-ocean ridge pillow basalts have both crystalline and glass components, and the glass crust is the most relevant to determining volatile degassing during ascent and extrusion. Previous work on the oxidation states of the mid-ocean ridge glasses [e.g., Christie et al. 1986] provides the opportunity to further investigate the relationship between degassing and changing oxidation state of the melt. The redox state of a magma is generally calculated as the ratio of ferric to ferrous iron in the melt and is controlled by equilibrium between C-O-H-S volatile species, their behavior during degassing, and mineral partitioning [Behrens & Gaillard 2006; Botcharnikov et al. 2005; Kress & Carmichael 1991; Christie et al. 1986]. As a result of volatile degassing the magmatic oxygen fugacity (fO_2) can be affected. When considering samples best suited to analyze the relationship of oxidation state and volatiles, MORBs are ideal due to their primitive composition as a result of having undergone simple magma evolution when compared to continental or ocean island basalts [Christie et al. 1986].

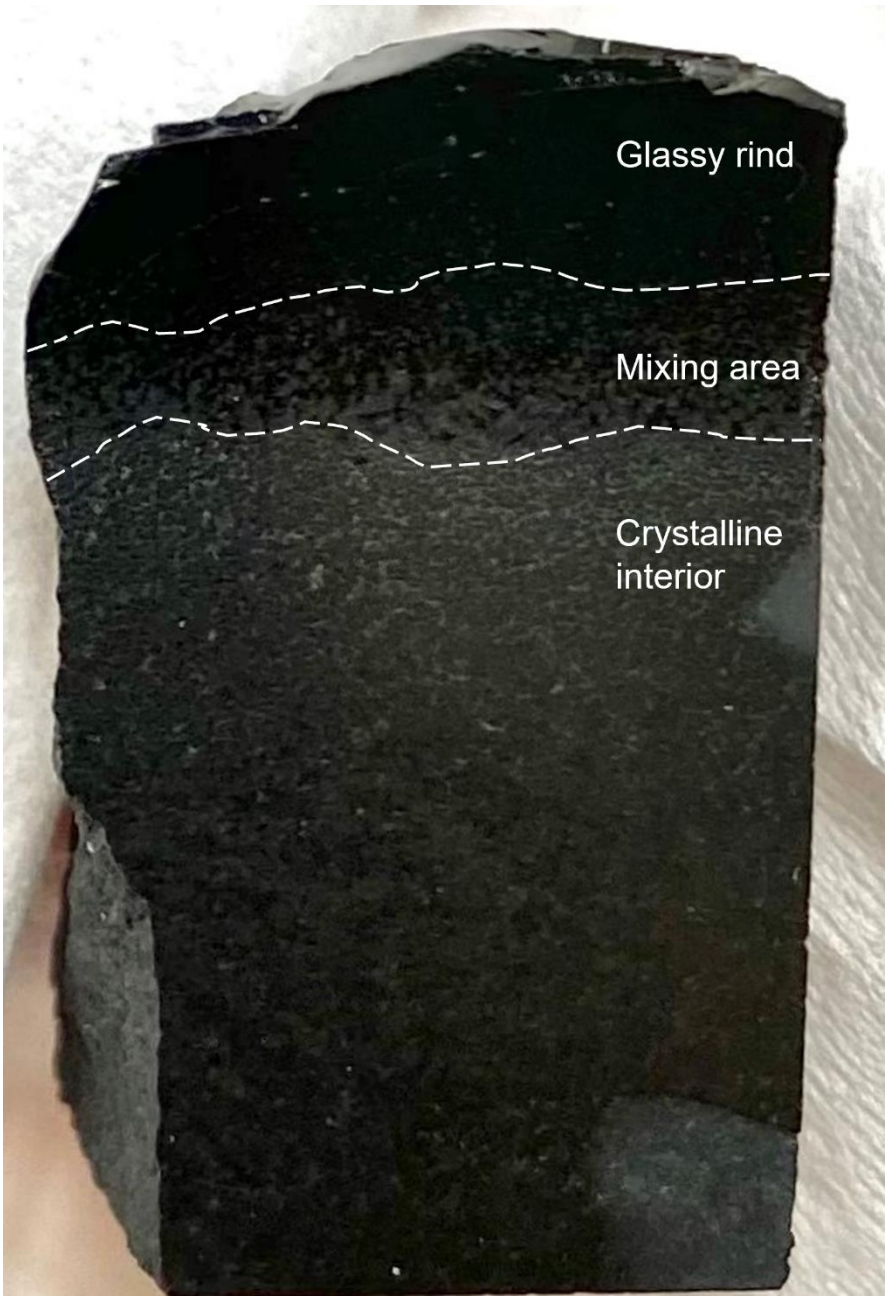

Figure 8. Image of ~1-inch tall, polished pillow basalt billet with the top black region being the glassy rind (black top material) that surrounds the crystalline interior (grey material) with a mixing area where the glass and crystals comingle.

FTIR

The FPA maps of the EPR pillow basalt sample show clear loss of hydration features at fractures, vesicles, and from the crystalline core to the glassy rim (Figure 9 & 10). In Figure 9, section A shows the influence of a fracture on the OH abundance with the cool toned diamond shapes indicating a stark depletion compared to the warm tones away from the fracture. Even the rimward abundance does not show such drastic differences in hydration abundance. Section B in Figure 9 shows both a core to rim trend of a lower hydration abundance at the rim. The fractures in section B indicate a similar trend to that of section A with a plain difference between the fracture associated abundances and the general trend of the glass far from the fractures. Figure 10 shows the abundance for smaller section C that allows for the influence of vesicles to be made clear. Since the map in section C does not span the entire length of the sample the effect of core to rim variation is mitigated to allow the vesicles (indicated by a pull away) to be seen. The difference in abundance between the vesicles and surrounding glass are not as substantial as the fractures, but still present a reliable method of hydration loss.

X-Ray Absorption Near-Edge Spectroscopy

Previous work by Lanzirotti et al. [2018] utilized multivariate analysis (MVA) to make use of the full X-ray absorption near-edge spectroscopy (XANES) spectral range in order to investigate the chemical state of vanadium (V) and iron (Fe) as functions of oxygen fugacity. Lanzirotti et al. [2018] used a combination of partial least-squares (PLS) regression and least absolute shrinkage and selection operator (Lasso) to predict the f_{O2} of equilibration in basaltic glasses from Kilauea and the East Pacific Rise. Their work returned values that indicated that their methods were a viable process for V oxybarometry configuration as they have a greater sensitivity to changes in f_{O2} at reduced redox conditions than just using Fe XANES alone. Lanzirotti et al. [2018] found rimward oxidation that correlates

to our findings of core to rim loss of hydration feature (Figure 11). Our data were collected on the sample EPR pillow basalt used in this study.

Hawaiian Glasses

Beads (Pele's Tears)

FTIR

The Pele's tear sample PHT1-HB2 contained both vesicles and fractures along with anhedral olivine in the center (Figure 12, Table 2). The FPA maps for PHT1-HB2 included areas of fracture (section A) and fracture with a vesicle (section B). Section A shows a depletion feature associated with the large fracture and smaller branching fractures. Section B shows an overall lower abundance of OH than section A as well as depletion features associated with the fracture and vesicle. The sample PHT1-HB2 indicates that fracture and vesicle hydration loss is effective and more pronounced than core to rim volatile loss.

EMPA

The EMPA data was plotted with findings of previous studies working with basaltic glass from Kilauea on a Total Alkali Silica (TAS) diagram (Figure 13; Table 3). The Pele's tears plotted similarly amongst themselves within our sample set and are consistent with previous literature values for basaltic compositions.

Rods (Pele's Hairs)

FTIR

The Pele's hair sample PHT1-PH4 has a FPA map of the central area of the hair with three fractures included (Figure 14). The largest fracture connects to the large vesicle at the top of the bead and exhibit significant depletion features associated with it. The second fracture is positioned at the top of the map near the center and shows minor influence on the abundance of OH. The third fracture is on the heel of the hair leftmost in the map and shows an associated depletion

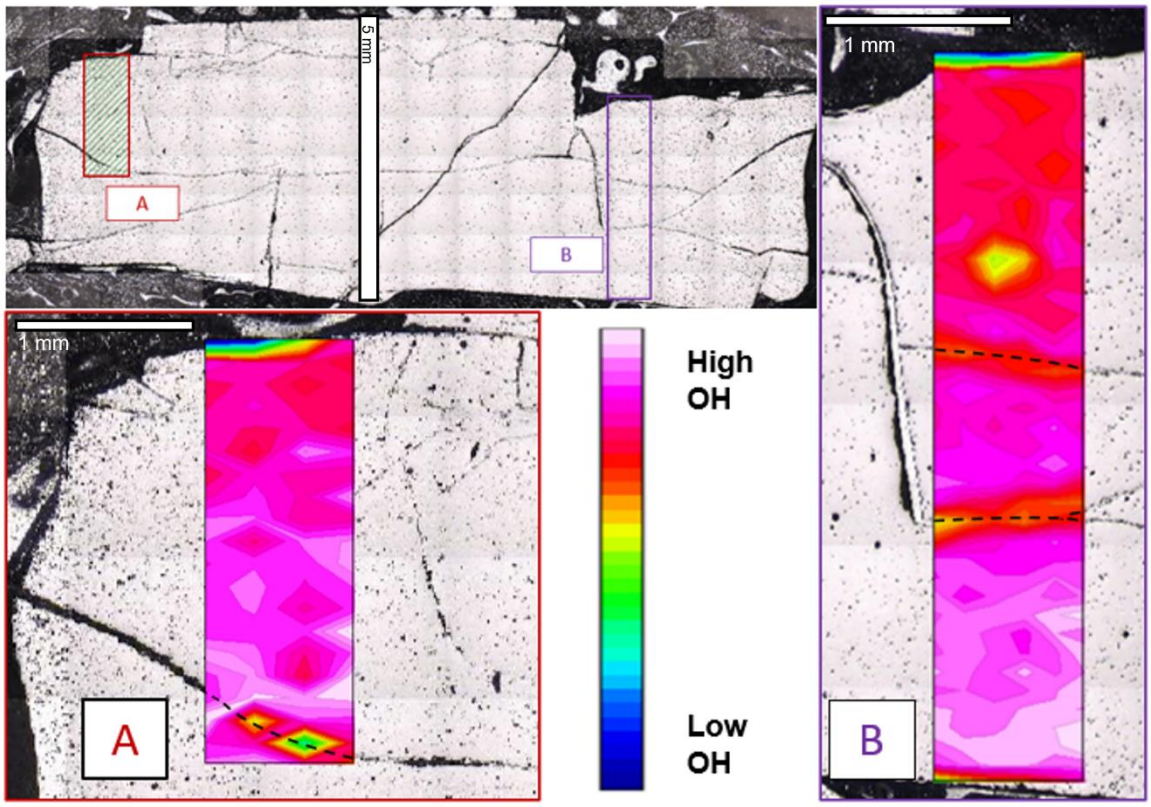

Figure 9. BSE micrograph of entire section (top left) and FPA hydration map of areas A (bottom right) & B (leftmost) of the pillow basalt with the cool toned features representing hydration depletion because of fracture and core to rim degassing.

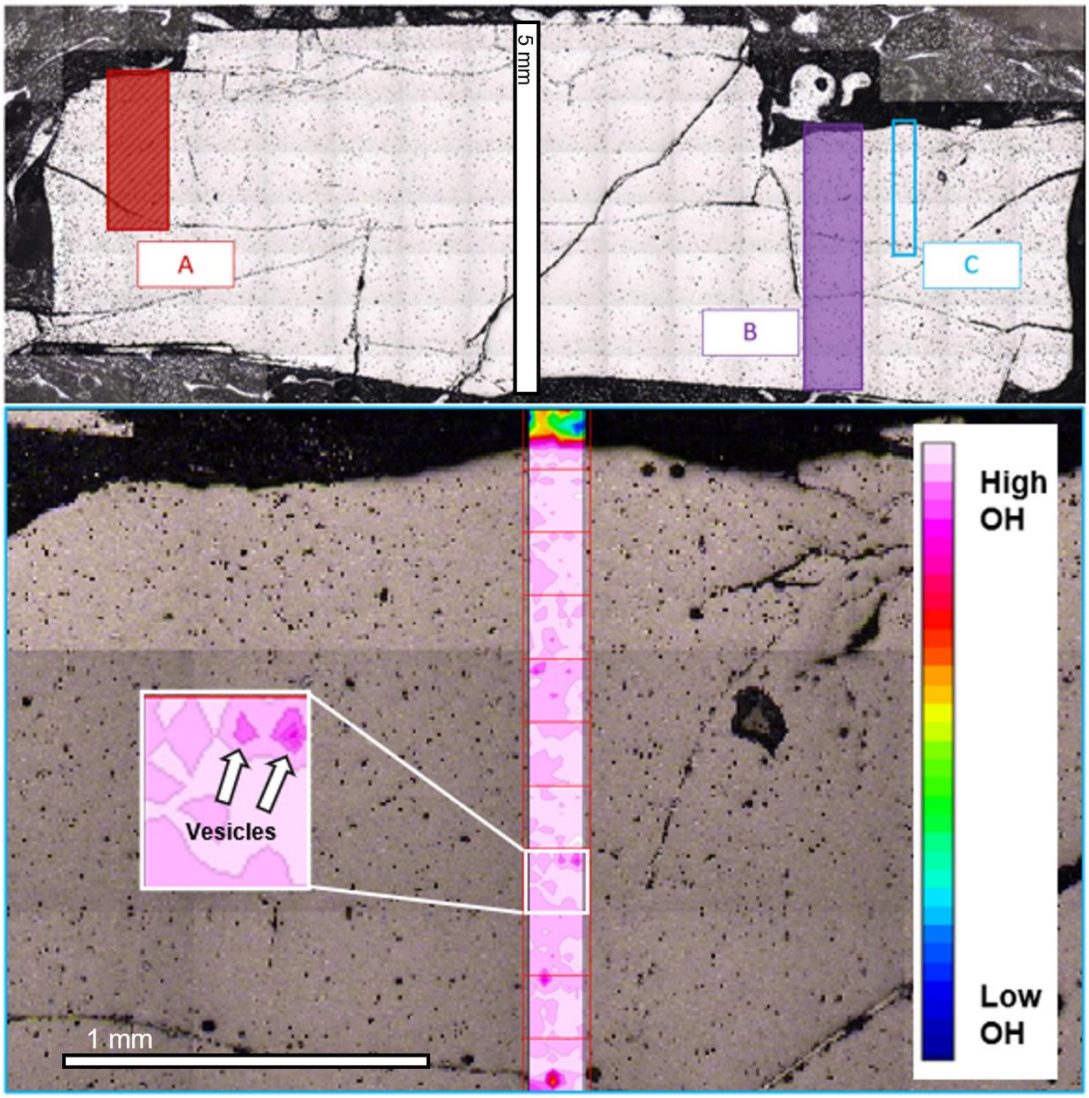

Figure 10. BSE micrograph of entire section (top) and FPA hydration map of area C (bottom) of the pillow basalt with the dark pink circular features representing hydration depletion because of vesicular degassing.

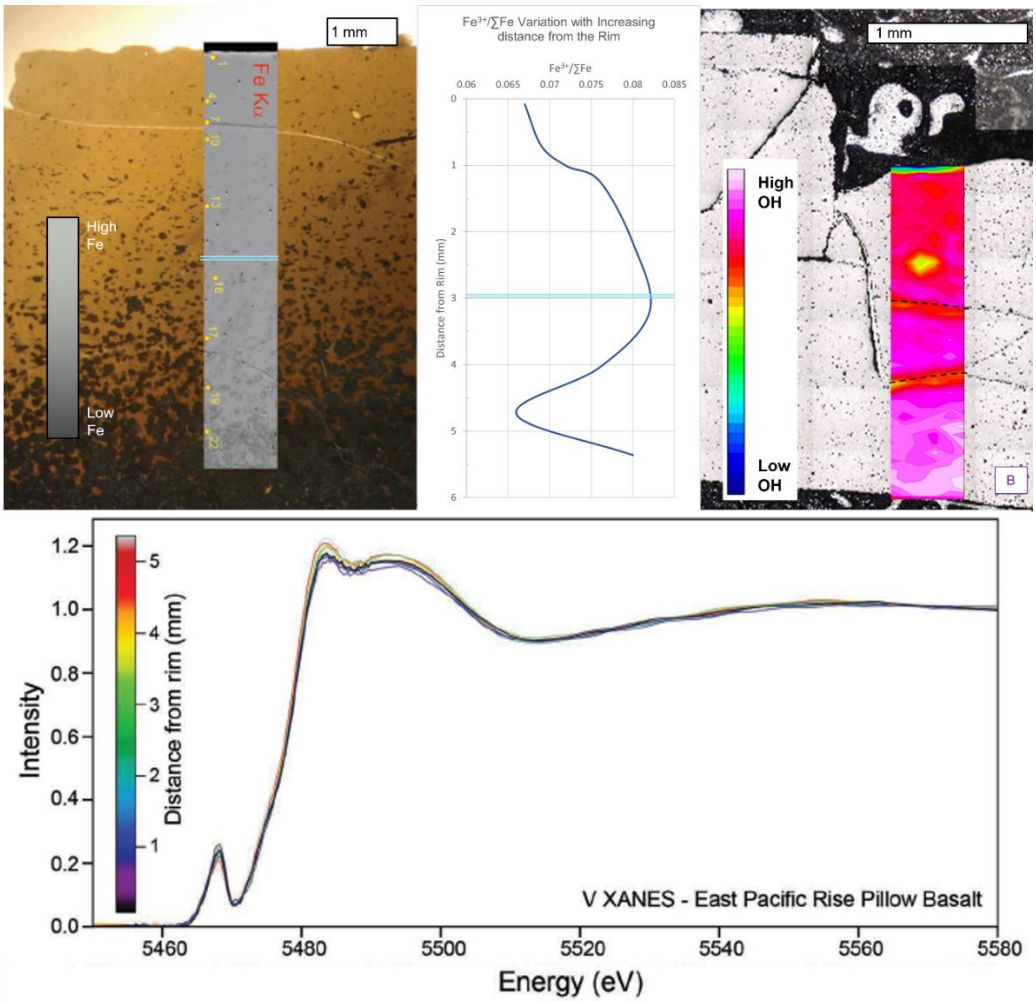

Figure 11. Leftmost image is modified from Lanzirotti et al. [2018] with high (white) and low (black) Fe fluorescence over a plane polarized light image of pillow basalt glass. The double blue line indicates the depth extent of the data in this study and the yellow points are areas selected for XANES analyses. The center plot is measured $Fe^{3+}/\sum Fe$ via XANES with increasing distance from the rim of the sample. On the right, Area B from Figure 7 is shown. The bottom spectra indicate the spread of V with increasing distance from the rim from Lanzirotti et al. [2018].

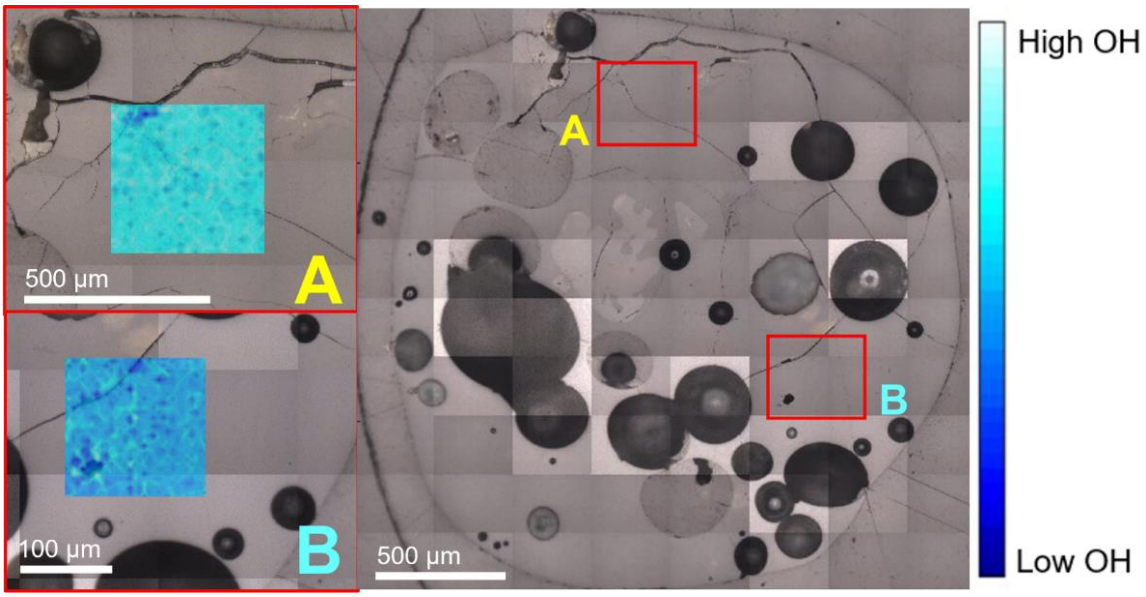

Figure 12. FPA hydration maps of areas A (top left) and B (bottom right) from sample PHT1-HB2.

Table 2. Weight oxide percent electron microprobe data for the crystal phases from the Pele's tears.

Sample	Point	SO3	P2O5	SiO2	TiO2	Al2O3	Cr2O3
HB-1	2	0.004	0	49.44	0.099	31.51	0
	10	0.003	0.032	50.137	0.058	31.178	0
HB-2	2	0.014	0.031	39.802	0.009	0.039	0.031
	3	0.005	0.032	39.226	0.065	0.04	0.042
	4	0	0.026	39.253	0.012	0.056	0.046

Sample	Point	MgO	CaO	MnO	FeO	Na2O	K2O	Total
HB-1	2	0.238	15.743	0.019	0.586	2.706	0.092	100.438
	10	0.274	15.155	0.009	0.72	2.922	0.12	100.608
HB-2	2	42.281	0.311	0.29	19.066	0	0.002	101.876
	3	42.269	0.317	0.233	18.916	0.002	0	101.148
	4	42.156	0.341	0.253	18.829	0	0.008	100.981

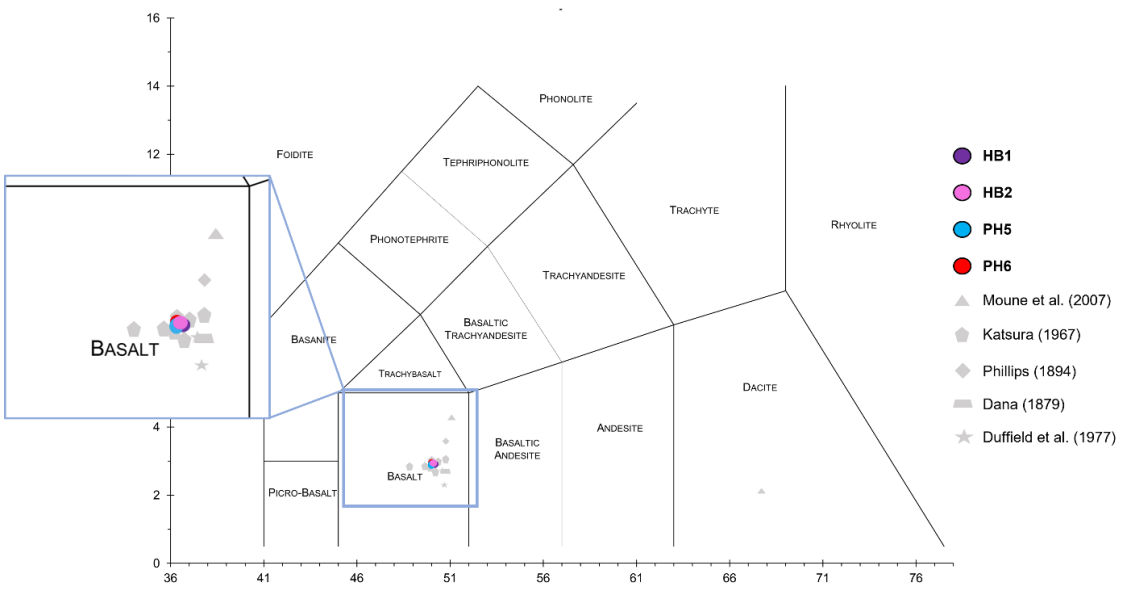

Figure 13. TAS diagram including electron microprobe data from this project (colored circled) and from previous studies Moune et al. (2007), Katsura (1967), Phillips (1894), Dana (1879), and Duffield et al. (1977) (grey shapes). The x-axis is SiO_2 and the y-axis is $Na_2O + K_2O$.

Table 3. Weight oxide percent electron microprobe values for glass points in Hawaiian samples.

Sample	Point	SO3	P2O5	SiO2	TiO2	Al2O3	Cr2O3	MgO	CaO	MnO	FeO	Na2O	K2O	Total
HB-1	1	0.04	0.315	50.155	2.853	13.486	0.05	6.76	11.182	0.171	11.106	2.326	0.533	98.976
	3	0.066	0.283	50.468	2.889	13.604	0.072	6.719	11.154	0.188	11.114	2.44	0.585	99.583
	4	0.032	0.302	50.147	2.834	13.682	0.031	6.813	10.989	0.169	11.077	2.273	0.563	98.913
	5	0.028	0.283	50.422	2.763	13.68	0.034	6.822	11.098	0.137	11.165	2.475	0.55	99.458
	6	0.028	0.26	50.404	2.79	13.406	0.066	6.824	11.149	0.185	11.133	2.263	0.55	99.058
	7	0.025	0.322	50.024	2.881	13.552	0.048	6.941	11.069	0.154	11.13	2.332	0.561	99.039
	8	0.065	0.273	50.167	2.832	13.723	0.069	6.765	11.142	0.177	11.08	2.302	0.556	99.151
	9	0.035	0.284	50.342	2.765	13.599	0.054	6.857	11.253	0.143	11.066	2.473	0.55	99.42
HB-2	1	0.033	0.287	50.204	2.802	13.771	0.059	6.678	11.215	0.166	11.086	2.422	0.596	99.319
	5	0.017	0.264	50.406	2.813	13.62	0.017	6.762	11.219	0.192	11.017	2.459	0.556	99.34
	6	0.036	0.298	50.201	2.902	13.544	0.036	6.731	11.277	0.15	11.115	2.371	0.59	99.252
	7	0.041	0.291	50.224	2.86	13.544	0.039	6.765	11.144	0.18	10.957	2.417	0.541	99
	8	0.025	0.275	50.298	2.832	13.55	0.072	6.826	11.228	0.154	10.946	2.396	0.512	99.112
	9	0.035	0.289	50.315	2.898	13.641	0.034	6.719	11.267	0.173	11.032	2.369	0.555	99.326
	10	0.05	0.3	50.247	2.802	13.628	0.023	6.922	11.266	0.186	11.048	2.318	0.542	99.334
PH-5	2	0.064	0.271	50.09	2.735	13.542	0.046	6.746	10.906	0.175	10.951	2.417	0.547	98.491
	3	0.027	0.337	49.94	2.708	13.466	0.029	6.807	10.979	0.157	10.902	2.418	0.557	98.327
	4	0.078	0.301	50.089	2.837	13.552	0.078	6.807	11.155	0.163	10.97	2.429	0.522	98.98
	5	0.086	0.299	49.957	2.69	13.444	0.053	6.642	10.974	0.175	10.908	2.367	0.562	98.158
PH-6	1	0.028	0.291	50.228	2.733	13.554	0.044	6.709	11.046	0.158	10.804	2.43	0.576	98.603
	2	0.058	0.312	50.05	2.808	13.467	0.05	6.654	11.013	0.166	10.712	2.288	0.547	98.125
	3	0.061	0.267	50.09	2.72	13.533	0.064	6.797	10.998	0.147	10.733	2.312	0.569	98.292
	4	0.041	0.29	50.182	2.834	13.51	0.05	6.839	11.147	0.191	10.789	2.294	0.558	98.726
	6	0.02	0.304	50.091	2.796	13.574	0.064	6.774	11.202	0.159	10.736	2.29	0.53	98.54

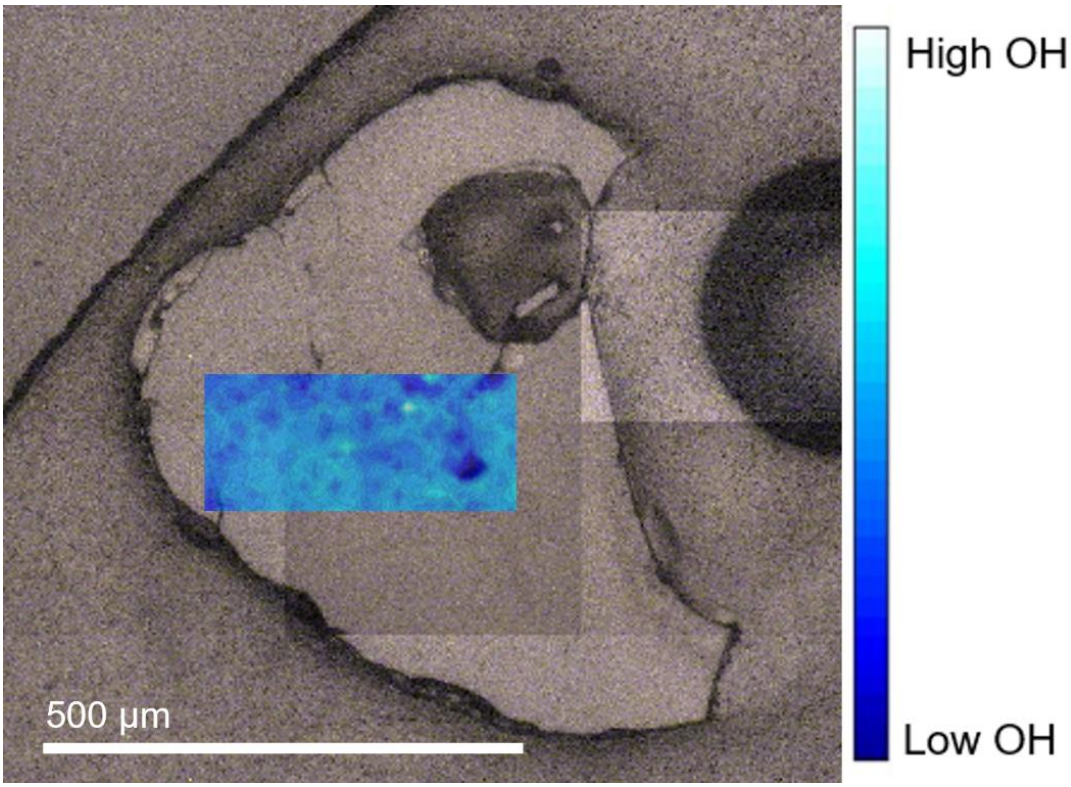

Figure 14. FPA hydration map of PHT1-PH4 over a reflected light image of the sample.

feature, though not as significant as the first fracture that feeds to the vesicle. The sample PHT1-PH4 indicates that for the Pele's hairs fractures serve as the most prominent areas of volatile loss.

EMPA

The geochemical data for the Pele's hairs are similar to that of the Pele's tears (Figure 13; Table 3). There were no crystalline structures found within the hairs and when compared to previous studies with samples from Kilauea the hairs in this study did not differentiate from the previous values.

Lunar Glasses

74220,226

Sample 74220 was collected during the Apollo 17 mission as an unconsolidated volcanic deposit located in the center of a trench on the south rim of Shorty crater (Figure 4) [Wolfe et al. 1981]. The unconsolidated material was sampled approximately 8 cm deep and contained orange glass spherules, glass shards, and partially crystallized spherules [Wolfe et al. 1981].

FTIR

Two beads were successfully analyzed from thin section 74220,226. Bead 1 is more elongate than bead 4 and has less cross-cutting fractures. The FPA map of Bead 1 shows an enrichment of OH near the fractured upper region of the bead and two depletion patterns near the center of the bead (Figure 15). There are also enrichment features along the rim of the bead around the entire circumference except for the lower right section of the bead that is heavily fractured. The lower right region shows a depletion associated with the fracturing. The FPA map of bead 4 returned some areas of unusable data (black box) caused by double reflection interference due to inadequate sample thickness (Figure 16). Also in Figure 16, there are two major areas of fracturing in the bead indicated, fractures and highly fractured areas. The FPA map indicates the OH depletions to be associated with the highly fractured areas and a mixed abundance with the fracture at the top of the bead. Bead 4 has an enrichment

feature at the bottom left area of the bead that is opposite the areas of fracture on the top center and top right areas.

15427,83

Sample 15427 was collected during the Apollo 15 mission on the northern rim of Spur crater and is from the same location as samples 15426 and 15425 (Figure 4) [Ryder 1985]. The sample is a loosely consolidated regolith breccia with friable clods of green tint that is largely due to the green volcanic glass concretions [Ryder 1985]. Within the sample, there is a mixture of light and dark matrix material consisting of impact melt glass and lithic fragments as well as yellow glass beads, green glass beads, mineral fragments, and glass shards [Ryder 1985].

FTIR

Two beads were analyzed from thin section 15427,83. Bead 2 has one complete cross-cutting fracture and bead 4 is devoid of fractures. In the FPA map of bead 2, the cross-cutting fracture is correlated with significant depletion features on either side of the fracture (Figure 17). There is also an enrichment on the right side of the fracture towards the top of the map and another strong enrichment on the left side of the fracture. There is a bend in the fracture towards the bottom of the bead that is associated with large depletions on both sides of the fracture. Bead 4 is smaller than bead 2 and has stronger OH signature. There is a concentric pattern to the OH features as there are no fractures to interrupt any degassing beyond the typical core to rim diffusion (Figure 18). The top portion of the bead displays depletion features along the rim; however, these are not representative of the glass itself as it is too thin to return reliable data. Figure 19 compares the FPA map of bead 4 with the calculated water concentration profile that spans the core to rim area indicated by the red box on the FPA. There is a steady decrease from the core to the bottom rim of the bead with a slight increase prior to the rim (Figure 19).

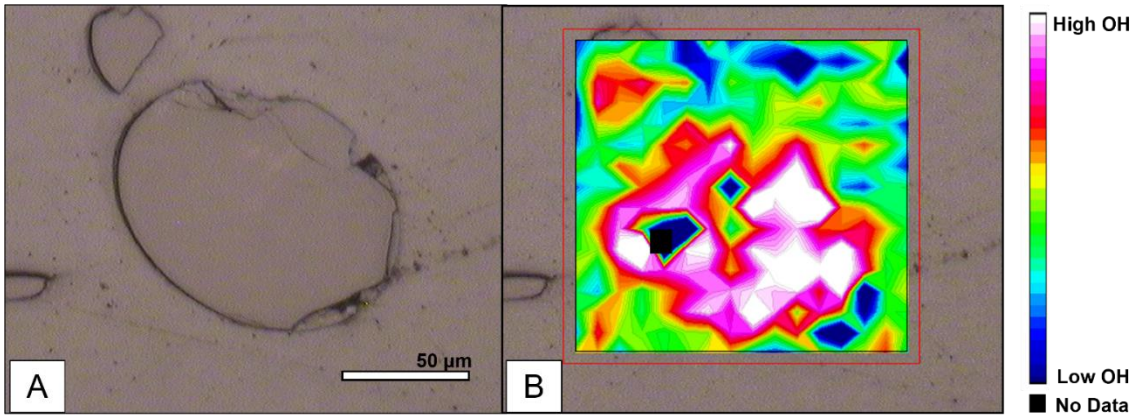

Figure 15. Reflected light image (left) and FPA of hydration features within bead 1 from sample 74220,226 (right)

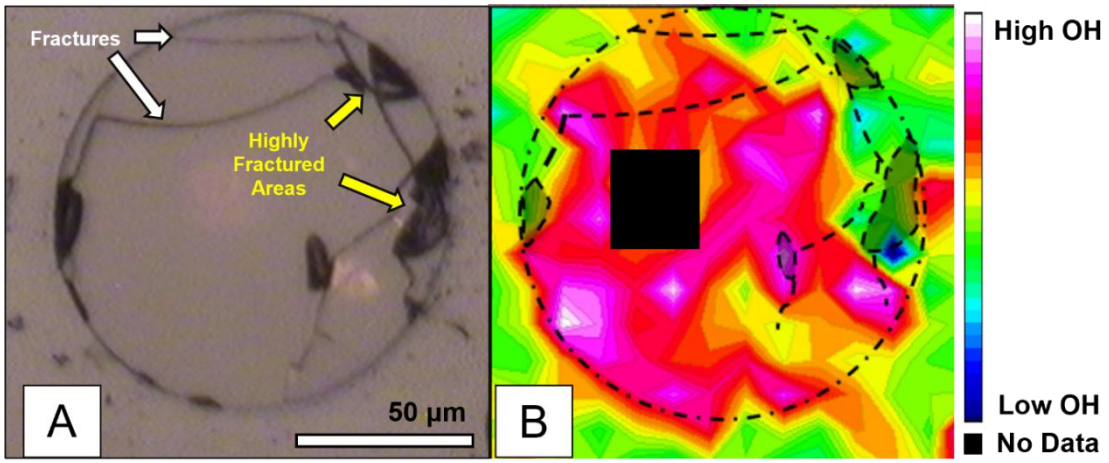

Figure 16. Reflected light image (left) and FPA of hydration features (right) within bead 4 from sample 74220,226 with areas of interest indicated with fracture labels and those heavily impacted by double reflection blacked out.

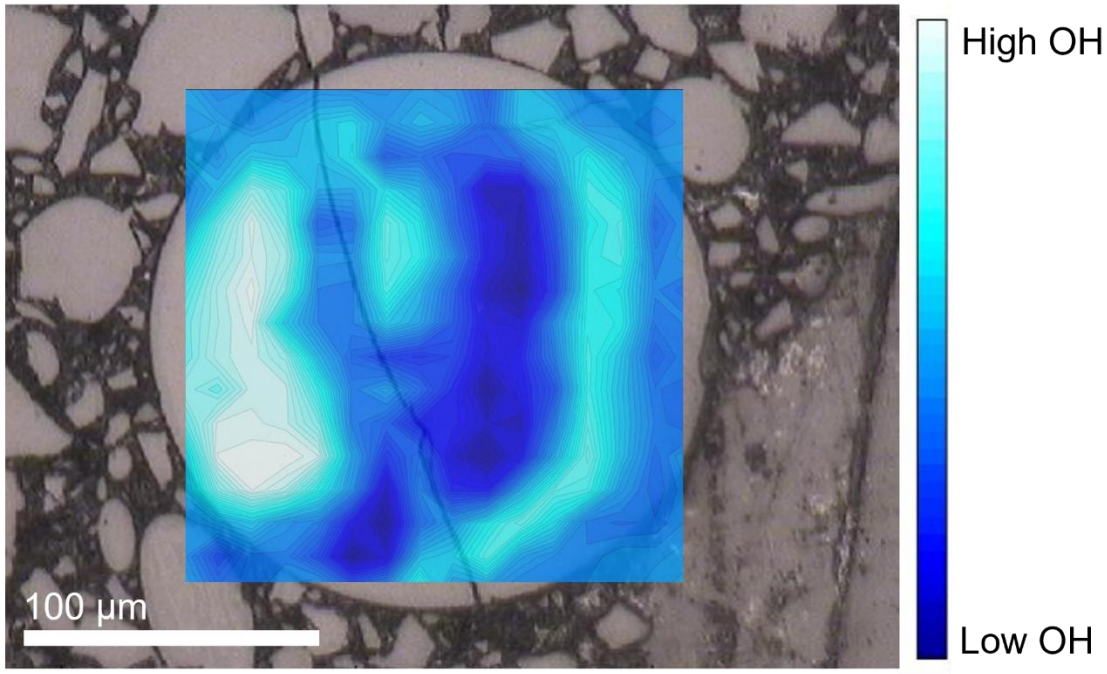

Figure 17. FPA of hydration features from bead 2 of sample 15427,83.

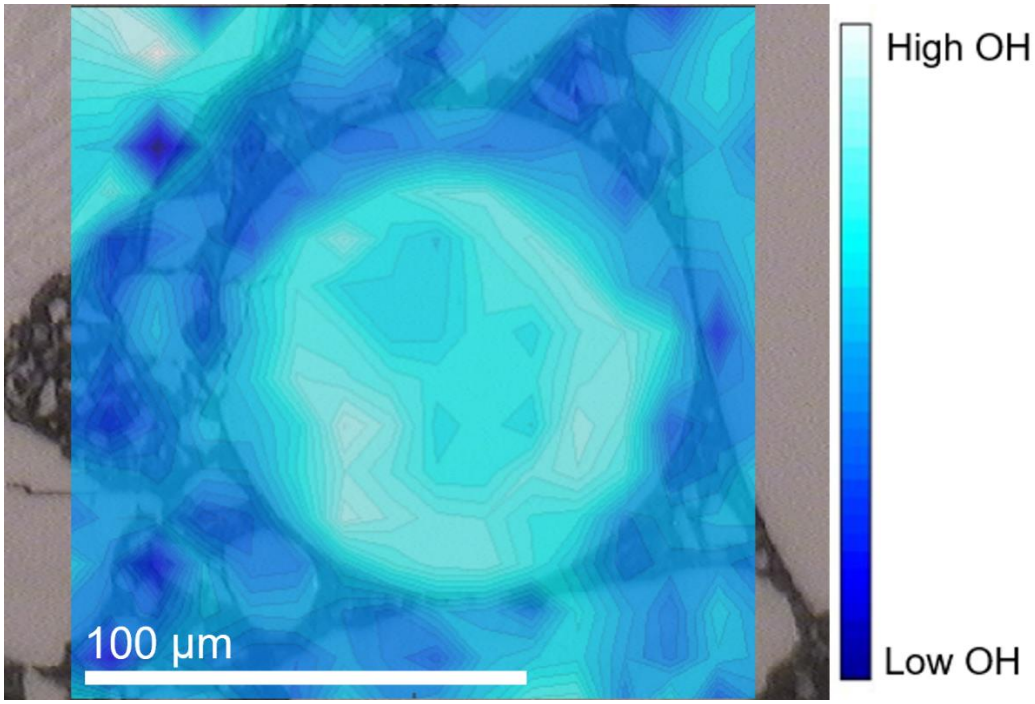

Figure 18. FPA of hydration map for bead 4 from sample 15427,83

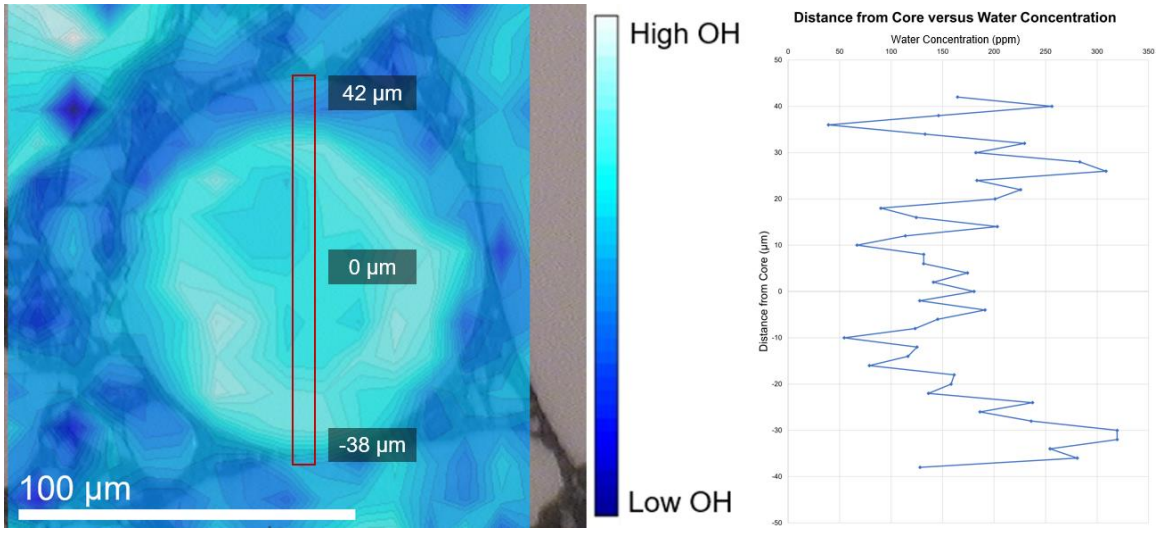

Figure 19. Sample 15427,83 bead 4 hydration FPA with area for concentration profile (left) and graph of distance from the core of the bead compared to calculated water concentration.

ANGSA: 73002,344

FTIR 73002,344A

Sample 73002,344A is from the most mature area of the core closest to the lunar surface being only 0.5-1.0 cm deep into the core (Table 4). The hydration features in the bead from the FPA indicate influence from the highly fractured areas along the rims of the bead and show a higher abundance of OH in the center of the bead even with the fractures (Figure 20).

FTIR 73002,344B

Sample 73002,344B is from the most mature area of the core closest to the lunar surface being only 0.5-1.0 cm deep into the core, same as sample 73002,344A (Table 4). The hydration features in the bead from the FPA indicate influence from the fractured area along the top rim of the bead on both the left and right sides (Figure 21). Water abundance calculations were done using the Beer-Lambert law to get the maximum and minimum values of 35 ppm and <0 ppm.

ANGSA: 73002,347

FTIR 73002,347A

Sample 73002,347A if from 1.0 to 1.5 cm deep in the core and is in the mature regolith (Table 4). The sample is partially crystallized and shows uniform low amounts of hydration features (Figure 22).

FTIR 73002,347B

Sample 73002,347B if from 1.0 to 1.5 cm deep in the core and is in the mature regolith (Table 4). The FPA of the bead shows clusters of hydration features and the reflected light image shows that the bead contains crystalline phases (Figure 23). Therefore, this bead is not entirely glass, and the crystal phases complicate the distribution of OH throughout the bead.

ANGSA: 73002,350

FTIR 73002,350A

Sample 73002,350A is from 2.5 to 3.0 cm deep into the core and is from the boundary layer with a mixture of mature and submature regolith (Table 4). The sample is extensively crystallized and shows massive depletion throughout the whole sample (Figure 24).

FTIR 73002,350C

Sample 73002,350C is from 2.5 to 3.0 cm deep into the core and is from the boundary layer with a mixture of mature and submature regolith (Table 4). The fragment contains crystalline features and vesicles throughout its elongated shape (Figure 25). There are depletion features near the two uppermost vesicles.

ANGSA: 73002,353

FTIR 73002,353A

Sample 73002,353A if from 5.0-5.5 cm deep in the core and is out of the mature regolith (Table 4). The sample is partially crystalline and has fractures at the top of the fragment (Figure 26).

ANGSA: 73002,355

FTIR 73002,355A

Sample 73002,355A is from 10-10.5 cm depth in the core and is furthest from the mature topsoil of the core (Table 4). The bead has one large vesicle on the left side that is associated with a depletion feature and has three prominent smaller vesicles that also contribute to depletion (Figure 27). The most enriched area of the bead the that in the bottom right, directly opposite the large vesicle.

FTIR 73002,355B

Sample 73002,355B is from 10-10.5 cm depth in the core and is furthest from the mature topsoil of the core (Table 4). The fragment contains crystalline phases along with glass pockets (Figure 28).

Table 4. ANGSA samples from core 73002 with the allocated splits in this study and their parent, depth, lithology, and size fraction.

Generic	Allocated Split	Parent	Depth (cm)	Lithology	Size Fraction (mm)
73002	,344	,18	0.5–1.0	Dark	<1 mm
73002	,347	,22	1.0–1.5	Dark	<1 mm
73002	,350	,34	2.5–3.0	Boundary	<1 mm
73002	,353	,1040	5.0–5.5	Light	<1 mm
73002	,355	,1079	10.0–10.5	Light	<1 mm
73002	,357	,1120	15.5–16.0	Light	<1 mm

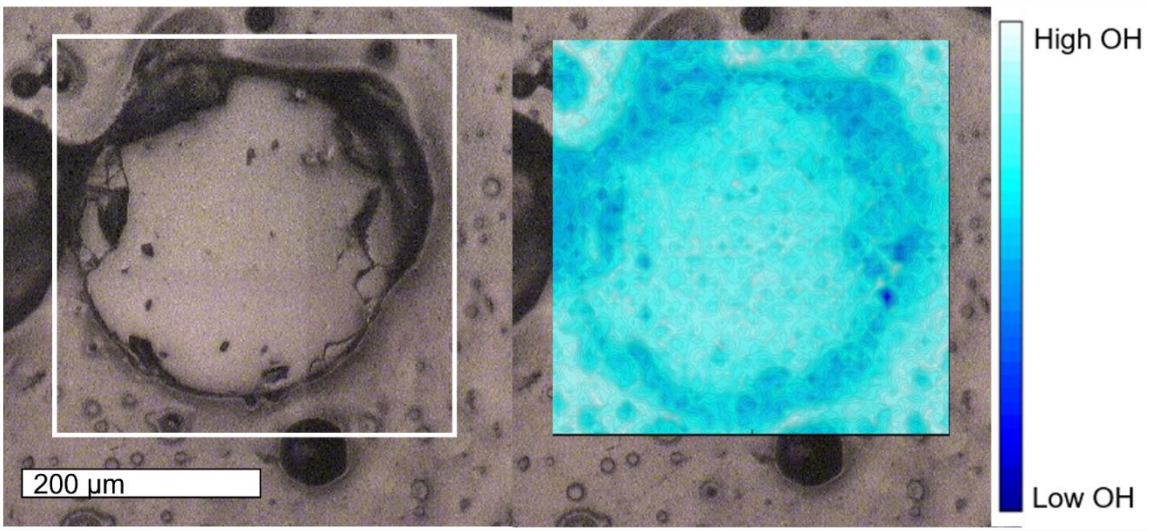

Figure 20. Sample 73002,344A reflected light image and extent of FPA map (left) and FPA hydration map (right).

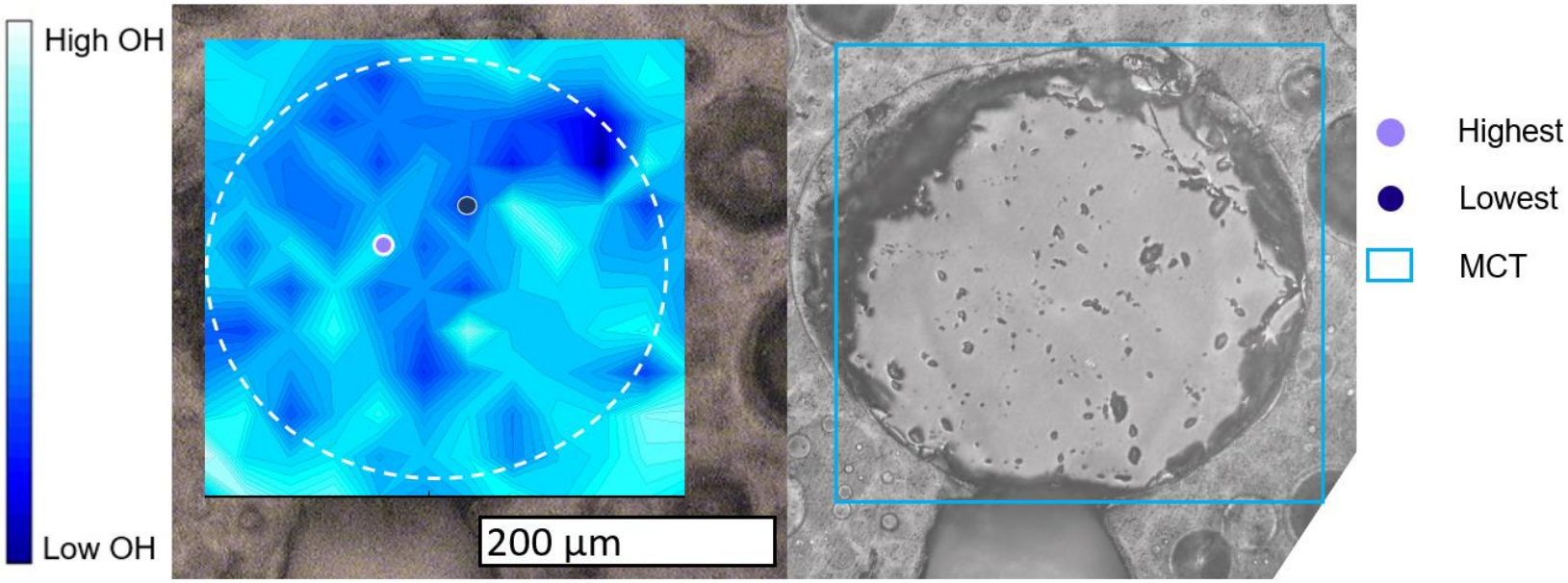

Figure 21. Sample 73002,344B MCT and location of points for water abundance calculations (right) and reflected light image with extent of MCT mapping (right).

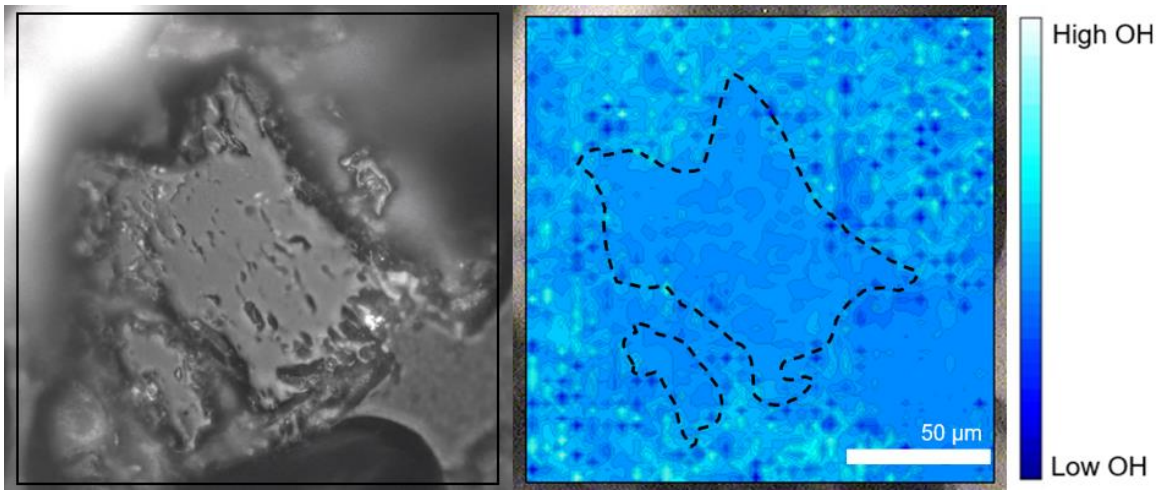

Figure 22. Sample 73002,347A reflected light (left) and FPA hydration map (right) with the fragment outlined by the black dotted line.

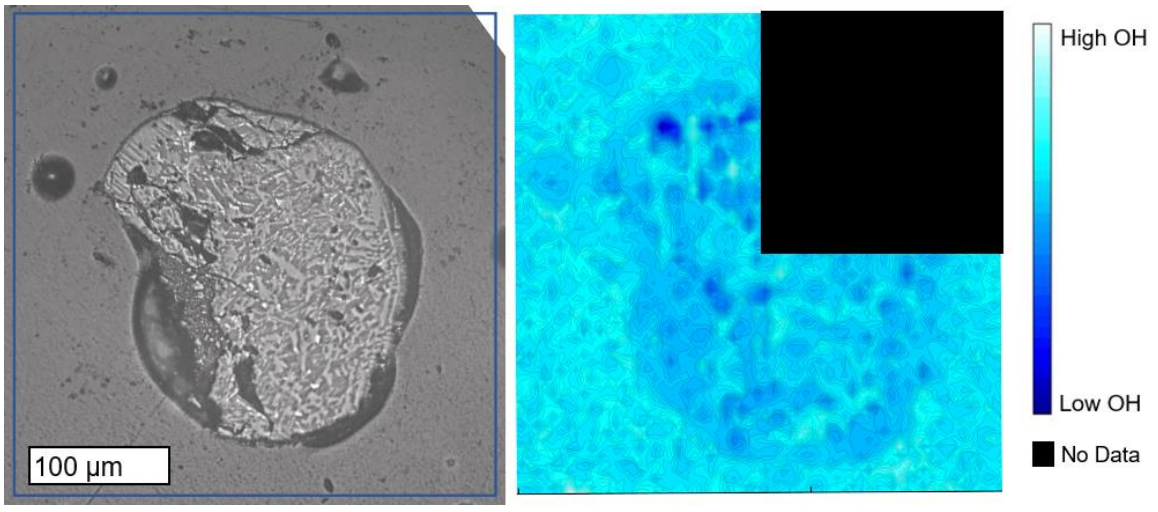

Figure 23. Sample 73002,347B reflected light image (left) and FPA hydration map (right) with the top right FPA block blacked out due to collection error.

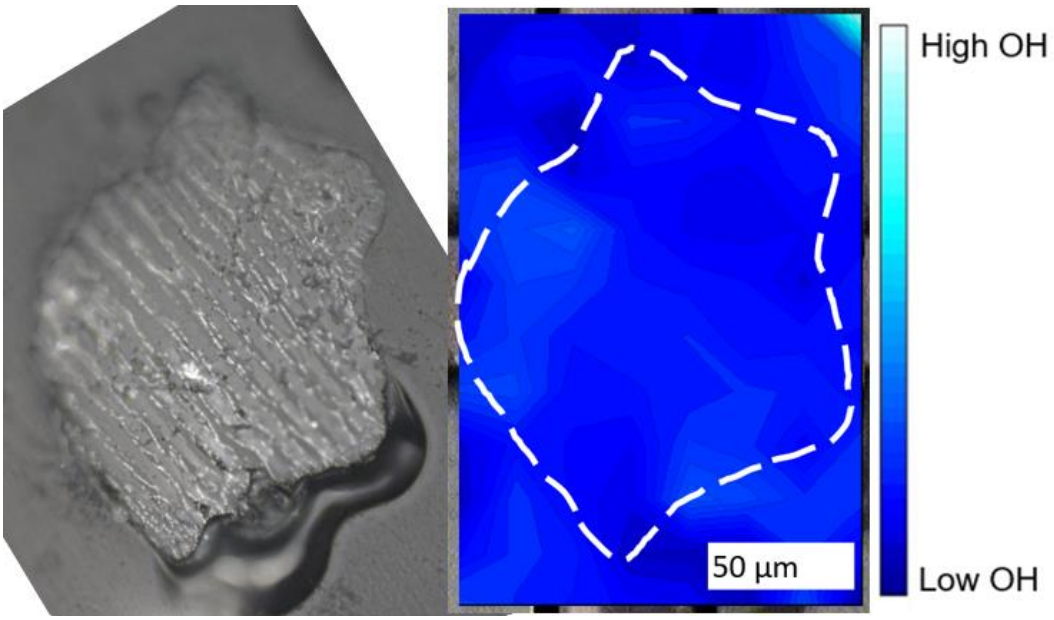

Figure 24. Sample 73002,350A reflected light (left) and MCT hydration map (right) with the fragment outlined in white.

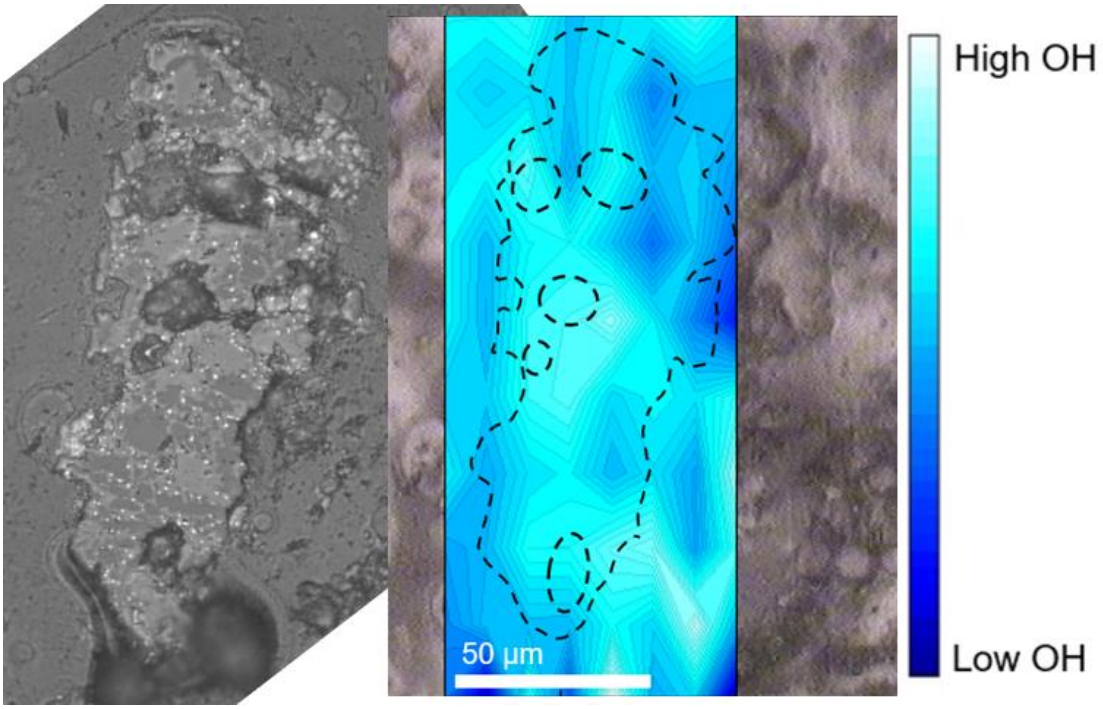

Figure 25. Sample 73002,350C in reflected light (left) and MCT hydration map (right) with the fragment outlined in the irregular black dotted line and vesicles indicated by black dotted circles.

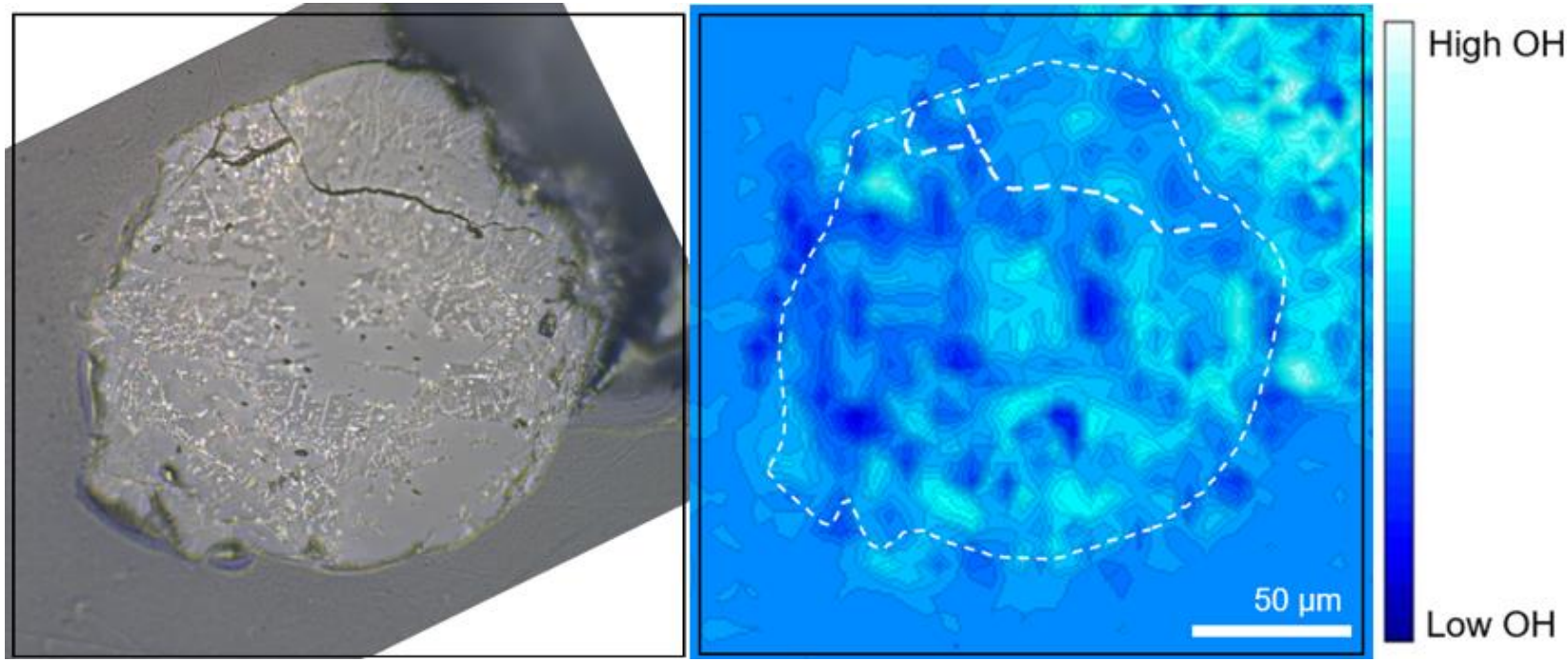

Figure 26. Sample 73002,353A reflected image (left) and FPA hydration map (right) with dotted irregular outline representing the border of the fragment and the dotted lines indicating fractures.

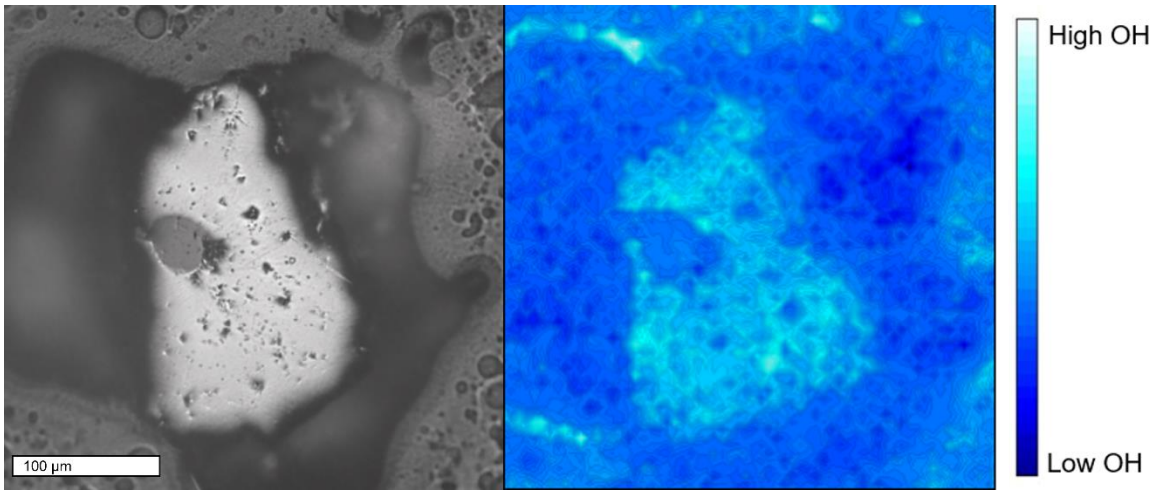

Figure 27. Sample 73002,355A reflected light image (left) and FPA hydration map (right).

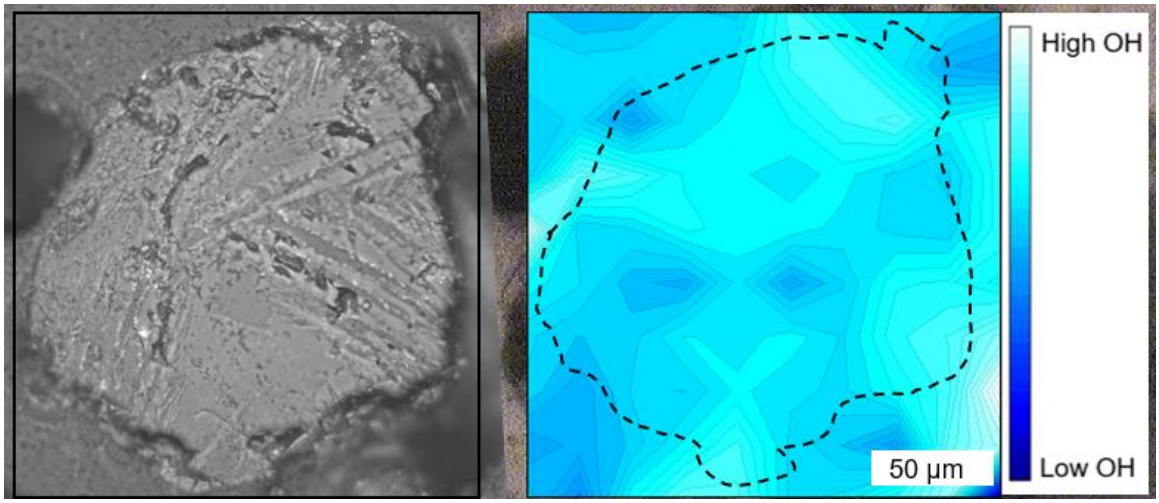

Figure 28. Sample 73002,355B reflected light image (left) and FPA hydration map (right) with fragment outline in dotted black line.

SECTION 5. DISCUSSION

Size Distribution

The size of the glass appears to exert a strong control over the types of degassing behavior of the sample. The difference in size between the Pele's tear, Pele's hair, and lunar samples is substantial. The largest sample is the pillow basalt, which cooled the slowest internally as evidenced by the crystalline interior. However, its glassy rind cooled as quickly as the other glasses (Figure 8). This sample provides the opportunity to examine volatile abundance in a glass that is under substantial pressure as the pillow basalt erupted on the sea floor. The larger size of the pillow basalt (5 mm wide) shows clear core to rim, vesicular, and fracture degassing with depletions of OH signatures in FTIR maps present. The second largest of the samples is the Pele's tear PHT1-HB2 (~1 mm diameter) which contains vesicles, fractures, and an anhedral olivine (Figure 12). Shimozuru [1994] discussed how the formation of tears can often lead to slower cooling time as they typically form from larger blebs of melt that do not have a high Pele's number. The low Pele's number is a reflection of the velocity of the bleb as it is ejected from the vent causing limited deformation of the spherical shape of the melt. The Pele's tears are not erupted with overbearing substantial pressure like the pillow basalt. Therefore, the fractures in the Pele's tears allow for more dramatic degassing evidence than the preexisting structures (vesicles) or core to rim.

The Pele's hair, PHT1-PH4, is smaller (~500 μm diameter) than PHT1-HB2 and does not contain any crystalline phases and hosts only one vesicle (Figure 14). The higher ejection velocity associated with Pele's hairs allows for a coalescing of multiple vesicles in the primary bleb into one and rapid quenching prohibits crystallization [Shimozuru 1994]. This process is summarized in Figure 3 with PHT1-HB2 representing panel A and PHT1-PH4 panel C. The smaller size of the Pele's hair and subsequent rapid quenching is shown by lesser influence of the fractures on OH depletion in FTIR maps and less prominent core to rim

degassing patterns. The hairs have a greater chance of trapping volatiles in the glass as they quenched much faster than the pillow basalt and tear. The quench time for the hair also may be closer to that of the glass beads from the lunar samples, based on their similar sizes.

The lunar samples can be broken down into two categories: the thin sections (74220,226 and 15427,83) and the ANGSA core thick sections (73002,344A, 73002,344B, 73002,347A, 73002,347B, 73002,350A, 73002,350C, 73002,353A, 73002,355A, and 73002,355B). The thin section samples present unique difficulties with using FTIR as they are not of uniform thickness which can result in unusable data. With this limitation in consideration, the general trends observed in both 74220,226 and 15427,83 are that in the absence of fractures the small beads quenched quickly enough to preserve OH features in the center of the bead (74220,226 bead 1 and 15427,83 bead 4) with a radial core to rim degassing pattern to the edge of the beads (Figure 15 & Figure 18). The larger beads (742220,226 bead 4 and 15427,83 bead 2) contain fractures that show influence on the distribution of the OH features in the FTIR FPA maps (Figure 16 and Figure 17). 74220,226 bead 4 has several fractures that greatly manipulated the degassing patterns to only permit interpretations based on these fractures. 15427,83 bead 2 has one large cross cutting fracture that clearly contributed to the OH degassing pattern in the FPA map near by a large depletion feature overlaying and surrounding the fracture. There are also areas of enrichment that show that the attempted degassing that was incomplete as a result of the bead quenching.

The ANGSA samples 73002,344A, 73002,344B, 73002,347A, 73002,347B, 73002,350A, 73002,350C, 73002,353A, 73002,355A, and 73002,355B are similar in size to the Apollo thin sections (50 to 200 µm). However, some of the samples host crystalline phases of iron oxides and mafic minerals (73002,347A, 73002,347B, 73002,350A, 73002,350C, 73002,353A, and 73002,355B) as well as vesicles (73002,350C and 73002,355A) (Figures 20 to 28). These result in complications to degassing mechanisms. The mineral

phases in 73002,347B correlate with intermediate hydration features in Figure 21; the glass areas are associated with strong depletion features indicating that the slower cooling rate that allowed for crystal growth provided ample time for complete degassing. In sample 73002,355A, the large vesicle is associate with a depletion feature, however, there are enrichment features in the bottom right area of the bead that indicate incomplete degassing (Figure 27). There are no crystal phases in 73002,355A, 73002,344A, or 73002,344B. The fractures along the rim of 73002,344A have associated depletion features and preservation of core enrichment (Figure 20). A similar pattern to 15427,83 bead 4 can be observed in 73002,344B in that there is evidence of core depletion and enrichment along the lower rim (Figure 19). This could indicate that the bead was able to entirely degas leaving the core depleted and rim enrichment representing in gassing from the surrounding hydrated vapor prior to quenching.

Terrestrial vs. Lunar

The Pele's tears display similarities and differences with the lunar beads. The tears exhibit an overall lower abundance of OH than the lunar beads. This can also be attributed to the slower cooling rate of the larger tears when compared to the much smaller lunar samples. Fractures and vesicles behave similarly as the lunar samples do with significant depletion features found near large fractures and vesicles (Figure 12).

The most similar to the lunar glass beads are the Pele's hairs, both in size and hydration behavior. The Pele's hairs are much smaller than the Pele's tears and cooled at similar rates to the lunar samples. This rapid quenching resulted in glasses with few or no vesicles, limited fracturing, and preserved enrichment features of OH (Figure 14). Sample 73002,344A (Figure 20) contains fractures that influence the distribution of OH in similar way to the fractures in sample PHT1-PH4 (Figure 14). This leads to the interpretation that of the terrestrial samples, the smallest glasses (Pele's hairs) that had similar formation conditions to the lunar beads likely are the most accurate analogues for volatile studies.

Apollo vs. ANGSA

Volatiles

The distribution of water in the glasses as seen by FTIR analyses between the Apollo thin sections and the fresh ANGSA beads are similar. The most prominent difference between the thin sections and the ANGSA beads is that the ANGSA samples include both crystalline phases and vesicles. This is likely the result of sample bias in the preparation of sample 74220,226 as the purely glass beads could have been favored for the thin section. Sample 15427,83 being a regolith breccia could make it more difficult to identify crystalline glass spherules from other clasts within the breccia, leading to bias for the easily spotted pure glass beads. The ANGSA beads were selected without the bias of knowing the interior contents prior to polishing that may explain the mix of pure glass and crystalline bearing glass beads.

Comparisons for calculated abundance between the thin section sample and ANGSA beads were simplified to an evaluation of 15427,83 bead 4 (Figure 18) and 73002,344B (Figure 21). The calculated water concentration between the highest area and lowest area varies greatly from 15427,83 bead 4 and 73002,344B (Table 5). Even at 15427,83 bead 4's most depleted point in the FPA map the water abundance is well above zero. However, 73002,344B's calculated water abundance does go below 0 in the most depleted areas of the MCT map. Negative absorbance results from the reference sample having much higher absorbance than the sample. The reference absorbs more than the sample which constitutes a negative absorbance that when put into the Beer-Lambert law produces a "negative" water concentration. The different mapping types (FPA for 15427,83 and MCT for 73002,344B) could be causing the difference in calculated abundance. This could also indicate that 15427,83 bead 4 completely degassed and then experienced an in-gassing event while in the eruptive plume prior to quench, with the support for this being the rim enrichment and core depletion features (Figure 19) that are absent in 73002,344B.

Alternatively, as the differences could be the result of sample preparation; 15427,83 is a thin section whereas 73002,344B is a polished thick section. Our results suggest that thick sections return the most reliable FTIR data. This is observed via the Si peak feature that occurs between 1000 cm^{-1} and 900 cm^{-1} being strongest in sections that are thicker than the penetration depth of light into the sample (10 μm) (Figure 7) [MacDonald et al. 2000]. Therefore, future sample analysis should focus on thick sections.

Space Weathering Effects

When considering the potential effects of space weathering on regolith samples returned from the Moon, the core samples from 73002 are a unique opportunity for direct analysis. Table 4 details the distribution and characteristics of the bead and fragments from the mature surficial layers (73002,344 and 73002,347), intermediate boundary layer (73002,350) and submature samples (73002,353 and 73002,355). An unanticipated challenge with the samples from the 73002 core was the variety of beads and fragments that are contained within the core. Therefore, our sample size includes purely glass, partially crystalline, and fully crystalline beads and fragments (Figures 20 to 28). This range of crystallinity makes it arduous to assess any implications of space weathering on the OH features observed via FTIR MCT or FPA maps as the highly crystalline fragments will innately exhibit lower abundance of OH due to slower cooling time and limited glass content. However, sample 73002,355A does not contain crystalline features and is located in the submature regolith and shows similar OH distributions to those in the mature regolith (73002,344A and 73002,344B) (Figure 29).

When comparing the mature regolith core samples 73002,344 and 73002,347 to those of the thin section lunar samples (15427,83 and 74220,226) there are evident similarities in the distribution of hydration in the beads. Sample 73002,344 contains two glass beads that are similar in shape and size to 15427,83 and 74220,226.

Table 5. Calculated water abundance for the highest and lowest regions in 15427,83 bead 4 (Figure 16) and 73002,344B (Figure 19).

Sample	Highest Water (ppm)	Lowest Water (ppm)
15427,83 Bead 4	319	54
73002,344B	35	<0

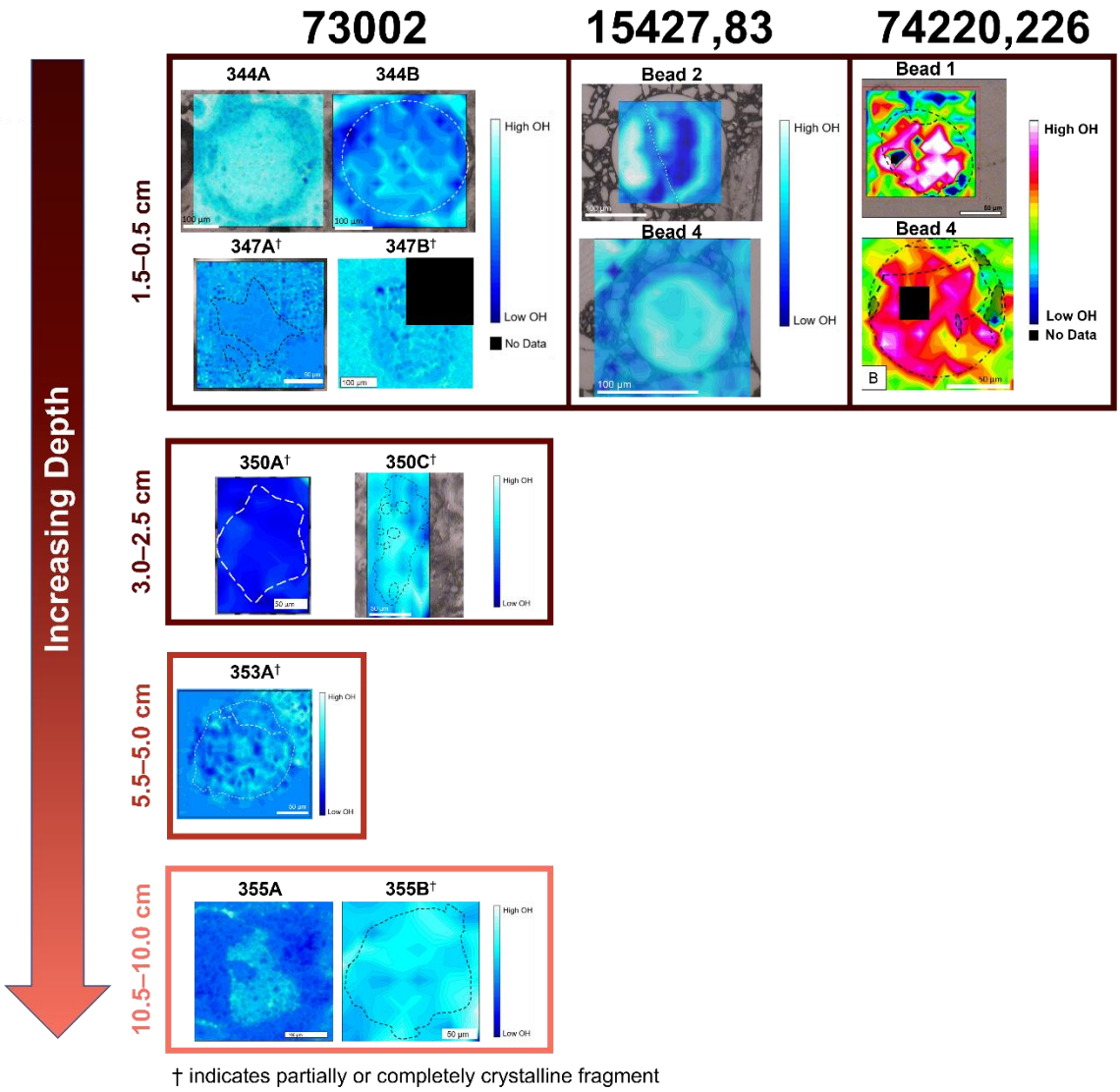

Figure 29. FPA and MCT maps for ANGSA, 15427,83, and 74220,226 glass beads and fragments (modified from Figures 13 to 27) throughout the space weathering profile from surface level with mature regolith (top box) to depth with submature regolith (bottom box) based on Figure 5 and Table 4.

Oxidation and Water

In the terrestrial MORB pillow basalt, V oxybarometry suggests that the f_{O2} varies from NNO–2.67 (±0.33) to NNO–3.72 (±0.33) with increasing distance away from the glassy rind (mean f_{O2} = NNO–2.62) [Lanzirotti et al. 2018]. The mean $Fe^{3+}/\sum Fe$ from Fe XANES is 0.074 which results in a f_{o2} of NNO–2.54 [Lanzirotti et al. 2018]. This is similar to the results from V oxybarometry, however, the f_{o2} values reported by Lanzirotti et al. [2018] are more reduced than some previous MORB estimates (NNO–2.0 and NNO–0.6 [e.g., Christie 1986]).

The rimward oxidation is relevant to this work as it may result from either the addition of oxygen to the melt or the loss of H_2O from rim to core via H diffusion. Both processes would result in increased melt oxidation from core to rim. This can be correlated with melt degassing from rim to core as measured via FTIR (Figure 11) in which higher abundances of hydration features are observed near the crystalline interior of the pillow basalt and lower abundances at the rim. This relationship between the changing oxidation state and loss of water via degassing during cooling of the basalt could be used to evaluate glasses where rapid volatile diffusion is complete, but the slower oxidation changes are still present.

SECTION 6. SUMMARY AND IMPLICATIONS

Products of explosive volcanism are used to ascertain pre-eruptive conditions as they may cool quickly enough to preserve initial volatile concentrations and offer insight into eruptive degassing processes. Therefore, utilizing samples like glass beads from fire-fountain style eruptions provides information pertaining to initial magmatic volatile contents.

In this study, Hawaiian glasses (Pele's hairs and tears), a pillow basalt, and lunar glass beads were analyzed to constrain geochemistry and abundance of water within the glasses. The degassing mechanism for water during eruption and cooling was observed to differ based on the size of the sample. The larger samples, the pillow basalt and Pele's tears (mm scale), appear to have cooled more slowly allowing for vesicles and fractures to provide the main degassing pathways, with minor core-to-rim degassing. The smaller glass samples (50–200 µm), like those of the lunar beads and Pele's hairs, contain less fractures and no or few vesicles and the effects of core-to-rim degassing are more evident.

Two types of lunar samples were analyzed: thin section (15427,83 and 74220,226) and ANGSA thick section (73002,344-347). The two types show differing responses to degassing based on water abundance calculations done. The ANGSA beads exhibited much lower abundances of water and have areas that show complete degassing (Table 5). Whereas the thin section sample 15427,83 has higher abundances of water and no areas of complete degassing (Table 5). The water abundance values for 15427,83 analyzed here are similar to the higher volatile values reported by Saal et al (2008), while the ANGSA values are on the lower end of their work. This may result from differences in sample thickness, thin vs. thick section, FPA vs. MCT mapping, and the pristine nature of the sample with regard to previous analysis. Section 15427,83 has been in circulation for years and experienced previous destructive analytical techniques on other areas of the thin section. While an effort was made to avoid the areas that had experienced prior analysis, repeated exposure to instruments like the

electron microprobe could have inadvertently altered the sample. This is especially true for highly volatile elements such as hydrogen [e.g., Renggli et al. 2017; Ustuniski et al. 2015; Moore 1970]. In addition to the age and circulation of the sample, because it is a thin section, it is inherently less effective for FTIR analyses due to the higher incidence of double reflection and spectral noise.

The ANGSA samples are ideal for investigating water degassing in lunar silicate glasses because they are fresh samples that were prepared as thick sections. This projects the necessity of a larger number of samples, as the limited samples included in our findings are inconclusive due to variety in crystallinity. Without the risk of prior analysis contamination and minimizing the impact of double reflection, the data returned from FTIR of the ANGSA samples are believed to be more representative of the sample.

SECTION 7. FUTURE WORK

This research indicates that the volcanic glasses rapidly quenched during explosive eruptions can contain measurable water. However, analyzing the water contents using FTIR mapping is difficult. In the future, increasing the sample size of the lunar glasses prepared from core 73002 and other ANGSA cores would be beneficial. With a larger number of samples, outliers can be identified and trends in the abundance of water and methods of lunar melt degassing can be better constrained. This will also likely raise the incidence of purely glass beads that are optimal for this work compared to partially or fully crystalline fragments.

Following FTIR analysis, more destructive analytical techniques, like electron microprobe and X-ray absorption near edge structure (XANES), can be undertaken to better understand potential geochemical correlations. Comparison of the XANES data for the Hawaiian and lunar glasses to the pillow basalt from Lanzirotti et al. [2018] would provide further insight into the relationship between changing oxidation state and melt degassing.

LIST OF REFERENCES

Anand, M., R. Tarte, & J. J. Barnes. Understanding the origin and evolution of water in the Moon through lunar sample studies. *Phil. Trans. R. Soc. A* 372.

Arndt, J. & E. von Engelhardt (1987) Formation of Apollo 17 Orange and Black Glass Beads. *Journal of Geophysical Research, 92*, B4, p. E372-E376.

BVSP (Basaltic Volcanism Study Project) (1981). Basaltic Volcanism on the Terrestrial Planets. Pergamon Press.

Behrens, H. & F. Gaillard (2006) Geochemical Aspects of Melts: Volatiles and Redox Behavior. *Elements, 2*, p. 275-280.

Bell, D. R. & G. R. Rossman (1992) Water in the Earth's Mantle: The Role of Nominally Anhydrous Minerals. *Science 255*, 5050, p. 1391-1397.

Botcharnikov, R. E., J. Koepke, F. Holtz, C. McCammon, & M. Wilke (2005) The effect of water activity on the oxidation and structural state of Fe in ferro-basaltic melt. *Geochimica et Cosmochimica Acta, 69*, p. 5071-5085.

Broz, P., H. Bernhardt, S. J. Conway, & R. Parekh (2021) An overview of explosive volcanism on Mars. *Journal of volcanology and geothermal research, 409*, p. 107125.

Cannata, C. B., R. De Rosa, P. Donato, S. Donato, G. Lanzafame, L. Mancini, & B. F. Houghton (2019) First 3D imaging characterization of Pele's hair from Kilauea volcano (Hawaii). *Sci Rep, 9,* 1711, p. 1-13.

Christie, D. M., I. S. E. Carmichael, & C. H. Langmuir (1986) Oxidation states of mid-ocean ridge basalt glasses. *Earth and Planetary Sci. Lett., 79*, p. 397-411.

Colin, A., P. Burnard, & B. Marty. Mechanisms of magma degassing at mid-ocean ridges and the local volatile composition (^{4}He-^{40}Ar-CO_2) of the mantle by laser ablation analysis of individual MORB vesicles. *Earth & Planetary Science Letters, 361,* p. 183-194.

Dana, J. D. (1879) On the composition of the capillary volcanic glass of Kilauea, Hawaii, called Pele's hair. *American Journal of Science, 104*, p. 134-135.
Delano, J. W. (1986) Pristine Lunar Glasses: Criteria, Data, and Implications. *Journal of Geophysical Research, 91*, B4, p. D201-D213.

Denevi, B. W., M. S. Robinson, A. K. Boyd, H. Sato, B. W. Hapke, & B. R. Hawke (2014) Characterization of space weathering from lunar reconnaissance orbiter camera ultraviolet observations of the Moon. *J. Geophys. Res. Planets, 11*, p. 976-997.

Dixon, J.E., E. Stopler, & J. Holloway (1995) An Experimental Study of Water and Carbon Dioxide Solubilities in Mid-Ocean Ridge Basaltic Liquids. Part I: Calibration and Solubility Models. *Journal of Petrology, 36*, p. 1607-1631.

Dixon, J. E. (1997) Degassing of alkalic basalts. *American Mineralogist, 82 (3-4)*, p. 368-378.

Duffield, W. A., E. K. Gibson, & G. H. Heiken (1977) Some characteristics of

Pele's Hair. *Jour. Research U.S. Geol. Survey*, 5, p, 93-101.
Elkins-Tanton, L. T. (2003) Magmatic processes that produced lunar fire fountains. *Geophysical Research Letters, 30*, 10, p. 1513.
Gaetani, G. A. & T. L. Grove (1998) The influence of water on melting of mantle peridotite. *Contrib. Mineral. Petrol. 131,* p. 323–346.
Gonnermann, H. M. & S. Mukhopadhyay (2007) Non-equilibrium degassing and a primordial source for helium in ocean-island volcanism. *Nature, 449, (7165),* p. 1037-1040.
Gose, J., E. Schmadicke, & A. Beran (2009) Water in enstatite from Mid-Atlantic Ridge peridotite: Evidence for the water content of the suboceanic mantle? *Geology, 37, (6)*, p. 543-546.
Guest, J. E. & J. B. Murray (1976) Volcanic features of the nearside equatorial lunar maria. *Journal of the Geological Society of London, 132*, p. 251-258.
Hapke, B. (2001) Space weathering from Mercury to the asteroid belt. Journal of Geophysical Research, 106, pp. 39-73.
Hauri, E. H. (2002) SIMS analysis of volatiles in silicate glasses, 2: Isotopes and abundances in Hawaiian melt inclusions. *Chemical Geology, 183, 1,* p. 115-141.
Hauri, E. H., T. Weinreich, A. E. Saal, M. C. Rutherford, & J. A. Van Orman (2011) High Pre-Eruptive Water Contents Preserved in Lunar Melt Inclusions. *Science, 333.*
Hauri, E. H., A. E. Saal, M. J. Rutherford, & J. A. Van Orman. (2015) Water in the Moon's interior: Truth and consequences. *Earth and Planetary Science Letters, 409*, 252-264.
Head, J. W. (1976) Lunar Volcanism in Space and Time. *Reviews of Geophysics and Space Physics, 12, 2,* p. 265-294.
Heide, F. & F. Wlotzka (1994) Meteorites; Messengers from Space. Springer-Verlag Berlin.
Heiken, G. & K. Wolhetz (1985) Volcanic Ash. University of California press, Berkeley, California.
Hiesinger & Head (2006) New Views of the Moon. *Reviews in Min. and Geochem.* 60, 1-81.
Hirth, G. & D. Kohlstedt (1996) Water in the oceanic upper mantle: implications for rheology, melt extraction and the evolution of the lithosphere. *Earth & Planetary Science Letters, 144*, p. 93–108.
Igami, Y., S. Muto, A. Takigawa, M. Ohtsuka, A. Miyake, K. Suzuki, K. Yasuda, & A. Tsuchiyama (2021) Structural and chemical modification of oxides and OH generation by space weathering: Electron microscopic/spectroscopic study of hydrogen-ion-irradiation. *Geochimica et Cosmochimica Acta, 315*, p. 61-72.
Javoy, M., F. Pineau & J. C. Alle`gre (1982) Carbon geodynamic cycle. *Nature, 300*, p. 171–173.
Johnson, E. A. & G. R. Rossman (2003) The concentration and speciation of hydrogen in feldspars using FTIR and 1H MAS NMR spectroscopy. *Am.*

Min. 88, p. 901-911.
Jung, H. Y. & S. Karato, S (2001) Water-induced fabric transitions in olivine. *Science, 293*, p. 1460–1463.
Kallio, E., S. Dyadechkin, P. Wurz, & M. Khodachenko (2019) Space weathering on the Moon: Farside-nearside solar wind precipitation asymmetry. *Planetary and Space Science, 166*, p. 9-22.
Katsura, T. (1967) Pele's hair as a liquid of Hawaiian tholeiitic basalts. *Geochemical Journal, 1,* p. 157-168.
Kingsley, R. H. & J.-G. Schilling (1995) Carbon in Mid-Atlantic Ridge basalt glasses from ^{288}N to ^{638}N: Evidence for a carbon-enriched Azores mantle plume. *Earth & Planetary Science Letters, 129,* p. 31–53.
Kress, V. C. & I. S. E. Carmichael (1991) The compressibility of silicate liquids containing Fe_2O_3 and the effect of composition, temperature, oxygen fugacity and pressure on their redox states. *Contrib. Mineral Pertrol., 108*, p. 82-92.
Lanzirotti, A., M. D. Dyar, S. Sutton, M. Newville, E. Head, CJ Carey, M. McCanta, L. Lee, P. L. King, & J. Jones (2018) Accurate predictions of microscale oxygen barometry in basaltic glasses using V *K*-edge X-ray absorption spectroscopy: A multivariate approach. *Am. Min.* 103, 1282-1297.
Macdonald, G. A. (1949) Petrography of the Island of Hawaii. *USGS Prof. Paper 214-D,* p. 51-96.
Macdonald, G. A. (1972) Volcanoes. Prentice-Hall, Englewood Cliffs, NewJersey.
MacDonald, S. A., C. R. Schardt, D. J. Masiello, & J. H. Simmons (2000) Dispersion analysis of FTIR reflection measurements in silicate glasses. *Journal of Non-Crystalline Solids, 275,* p. 72-82.
Mandeville, C., J. Webster, M. Rutherford, B. Taylor, A. Timbal, & K. Faure (2002) Determination of molar absorptivities for infrared absorption bands of H_2O in andesitic glasses. *American Mineralogist, 87*, p. 813-821.
Matsumoto, T., T. Noguchi, Y. Tobimatsu, D. Harries, F. Langenhorst, A. Miyake, & H. Hidaka (2021) Space weathering of iron sulfides in the lunar surface environment. *Geochimica et Cosmochimica Acta, 299*, p. 69-84.
McCanta, M. C., M. D. Dyar, M. J. Rutherford, A. Lanzirotti, S. R. Sutton, & B. J. Thomson (2019) In situ measurement of ferric iron in lunar glass beads using Fe-XAS. *Icarus, 285*, p. 95-102.
McIntosh, I., A. Nichols, K. Tani, & E. Llewellin (2017) Accounting for the species-dependence of the 3500 cm^{-1} H_2O infrared molar absorptivity coefficient: Implications for hydrated volcanic glasses. *American Mineralogist, 102*, p. 1677-1689.
McSween, H. (1999) Meteorites and their Parent Planets. Cambridge University Press.
Mittal, T. & M. A. Richards (2018) Volatile Degassing from Magma Chambers as a Control on Volcanic Eruptions. *Journal of Geophysical Research: Solid Earth, 124,* p. 7869-7901.

Moore, J. G. (1970) Water Content of Basalt Erupted on the Ocean Floor. *Contr. Mineral. And Petrol., 28*, p. 272-279.
Morbidelli, A., J. Chambers, J. I. Lunine, J. M. Petit, F. Robert, G. B. Valsecchi, & K. E. Cyr (2010) Source regions and timescales for the delivery of water to the Earth. *Meteoritics & Planetary Science, 35*, p. 1309-1320.
Moune, S., F. Faure, P-J. Gauthier, & K. W.W. Sims (2007) Pele's hair and tears: Natural probe of volcanic plume. *Journal of Volcanology and Geothermal Research, 164*, p. 244-253.
Niedermann, S., W. Bach, & J. Erzinger (1997) Noble gas evidence for a lower mantle component in MORBs from the southern East Pacific Rise: Decoupling of helium and neon isotope systematic. *Geochimica et Cosmochimica Acta, 61, 13,* p. 2697-2751.
Nielsen, C. & H. Sigurdsson (1981) Quantitative methods for electron microprobe analysis of sodium in natural synthetic glasses. *American Mineralogist, 66*, p. 547-552.
Ohlhorst, S., H. Behrens, & F. Holtz (2001) Compositional dependence of molar absorptivities of near-infrared OH- and H_2O bands in rhyolitic to basaltic glasses. *Chemical Geology, 174*, p. 5-20.
Parfitt, E. A. & L. Wilson (1995) Explosive volcanic eruptions – IX. The transition between Hawaiian-style lava fountaining and strombolian explosive activity. *Geophys. J. Int., 121,* p. 226-232.
Parker, M., C. Agee, M. Duncan, & W. Westrenen (2011) Compressibility of molten Apollo 17 orange glass and implications for density crossovers in the lunar mantle. *Geochimica et Cosmochimica Acta, 75*, p. 1161-1172.
Paonita, A. & M. Martelli (2006) Magma dynamics at mid-ocean ridges by noble gas kinetic fractionation: assessment of magmatic ascent rates. *Earth & Planetary Science Letters, 241, 1-2,* p. 138-158.
Paonita, A. & M. Martelli (2007) A new view of the He-Ar-CO_2 degassing at mid-ocean ridges: homogenous composition of magmas from the upper mantle. *Geochimica Acta Cosmochimica, 71, 7,* p. 1747-1763.
Pearson, D., F. Brenker, F. Nestola, J. McNeill, L. Nasdala, M. Hutchinson, S. Matveev, K. Mather, G. Silvermit, S. Schmitz, B. Vekemans, & L. Vincze (2014) Hydrous mantle transition zone indicated by ringwoodite included within diamond. *Nature, 507*, p. 221-223.
Peck, D. L., T. L. Wright, & J. G. Moore (1966) Crystallization of tholeiitic basalt in Alae lava lake, Hawaii. *Bulletin Volcanologique, 29*, p. 629-655.
Peng, N., Y. Zhang, S. Chen, & J. Gagnon (2019) A melt inclusion study on volatile abundances in the lunar mantle. *Geochimica et cosmochimica acta, 249*, p. 17-41.
Philpotts, A. & J. Ague (2009) Principles of Igneous and Metamorphic Petrology. Cambridge University Press.
Phillips, A. H. (1894) A recent analysis of Pele's Hair and a Stalagmmite from the lava Caves of Kilauea. *American Journal of Science, 282*, p. 473-474.
Renggli, C. J., P. L. King, R. W. Henley, & M. D. Norman (2017) Volcanic gas

composition, metal dispersion and deposition during explosive volcanic eruptions on the Moon. *Geochimica et Cosmochimica Acta, 206*, p. 296-311.
Rutherford, M. J. & P. Papale (2009) Origin of basalt fire-fountain eruptions on Earth Versus the Moon. *Geology, 37*, 3, p. 219-222.
Ryder, G. (1985) Catalog of Apollo 15 Rocks. *Curatorial Branch Publication, 72*.
Saal, A. E., E. H. Hauri, C. H. Langmuir, & M. R. Perfit (2002) Vapour undersaturation in primitive mid-ocean-ridge basalt and the volatile content of earth's upper mantle. *Nature, 419, 6909*, p. 451-455.
Saal, A. E., E. H. Hauri, M. Lo Cascio, J. A. Van Orman, M. C. Rutherford, & R. F. Cooper (2008) Volatile content of lunar volcanic glasses and the presence of water in the Moon's interior. *Nature, 454*.
Schmincke, Hans-Ulrich (2004) Volcanism. Springer Berlin Heidelberg, New York.
Schultz, P.H. (1976) Moon Morphology. University of Texas Press, Austin, TX.
Seaman, S. J., M. D. Dyar, N. Marinkovic, & N. W. Dunbar (2006) An FTIR study of hydrogen in anorthoclase and associated melt inclusions. *Am. Min*. *91*, p. 12-20.
Sharp, Z. D., F. M. McCubbin, C. K. Shearer (2013) A hydrogen-based oxidation mechanism relevant to planetary formation. *Earth & Planetary Science Letters, 380*, p. 88-97.
Shearer, C. K., J. J. Papike, K. C. Galbreath, & N. Shimizu (1991) Exploring the lunar mantle with secondary ion mass spectrometry: a comparison of lunar picritic glass beads from the Apollo 14 and Apollo 17 sites. *Earth and Planetary Science Letters, 102*, 2, p. 134-147.
Shimozuru, D. (1994) Physical parameter governing the formation of Pele's hair and tears. *Bulletin of Volcanology, 56*, p. 217-219.
Simons, K., J. E. Dixon, J.-G. Schilling, R. Kingsley, & R. Poreda (2002) Volatiles in basaltic glasses from the Easter-Salas y Gomez seamount chain and Easter microplate: implications for geochemical cycling of volatile elements. *Geochemistry Geophysics Geosystems, 3, 7,* p. 1-29.
Sorby, H. C. (1877) Pele's Hair. *Nature, 16*, p. 23.
Stopler, E. (1982) Water in Silicate Glasses: An Infrared Spectroscopic Study. *Contributions to Mineralogy and Petrology, 81*, p. 1-17.
Swanson, D. A., T. R. Rose, A. E. Mucek, M. O. Garcia, R. S. Fiske, & L. G. Mastin (2014) Cycles of explosive and effusive eruptions at Kilauea Volcano, Hawaii. *Geology (Boulder), 42*, 7, p. 631-634.
Taylor, S. R. (1982) Planetary Science: A Lunar Perspective. *Lunar and Planetary Institute*.
Thomas, R. J., D. A. Rothery, S. J. Conway, & M. Anand (2014) Long-lived explosive volcanism on Mercury. *Geophys. Res. Lett., 41*, p. 6084-6092.
Ustunisik, G., H. Nekvasil, D. H. Lindsley, & F. M. McCubbin (2015) Degassing pathways of Cl-, F-, H-, and S- bearing magmas near the lunar surface: Implications for the composition and Cl isotopic values of lunar apatite.

American Mineralogist, 100, p. 1717-1727.
Vander Kaaden, K., C. Agee, & F. McCubbin (2015) Density and compressibility of the molten lunar picritic glasses: Implications for the roles of Ti and Fe in the structures of silicate melts. *Geochimica et Cosmochimica Acta, 149*, p. 1-20.
von Aulock, F.W., B.M. Kennedy, C.I. Schipper, J.M. Castro, D.E. Martin, C. Oze, J.M. Watkins, P.J. Wallace, L. Puskar, F. Begue, A.R.L. Nichols, & H. Tuffen (2014) Advances in Fourier transform infrared spectroscopy of natural glasses: Form sample preparation to data analysis. *Lithos, 206-207*, p. 52-64.
Wasson, J. T., W. V. Boynton, G. W. Kallemeyn, L. L. Sundberg, & S. M. Wai. (1976) Volatile Compounds released during lunar lava fountaining. *Lunar Sci. Conf.* p. 1583-1595.
Weider, S. Z., L. R. Nittler, S. L. Murchie, P. N. Peplowski, T. J. McCoy, L. Kerber, C. Klimczak, C. M. Ernst, T. A. Goudge, R. D. Starr, N. R. Izeneberg, R. L. Klima, & S. C. Solomon (2016) Evidence from MESSENGER for sulfur- and carbon-driven explosive volcanism on Mercury. *Geophys. Res. Lett., 43*, 8, p. 3653-3661.
Weston, B., R. Burgess, & C. Ballentine (2015) Disequilibrium degassing model determination of the $^{3}He/^{22}Ne$ of the MORB and OIB mantle sources. *Earth & Planetary Science Letters, 410,* p. 128-139.
Wetzel, D. T., E. H. Hauri, A. E. Saal, & M. J. Rutherford (2015) Carbon content and degassing history of the lunar volcanic glasses. *Nature, 8*, 755-761.
Wiesli, R., B. Beard, L. Taylor, & C. Johnson (2003) Space weathering processes on airless bodies: Fe isotope fractionation in the lunar regolith. *Earth and Planetary Science Letters*, 2016, p. 457-468.
Wilson, L. & J. W. Head (1981) Ascent and eruption of basaltic magma on the Earth and Moon. *J. Geophys. Res., 86,* p. 2971-3001.
Wilson, L. & J. W. Head (2017) Generation, ascent and eruption of magma on t he Moon: New insights into source depths, magma supply, intrusions, and effusive/explosive eruptions (Part 1: Theory). *Icarus,283*, p. 146-175.
Wolfe, E., N. Bailey, G. Bailey, B. Lucchitta, W. Muehlberger, D. Scott, R. Sutton, & H. Wilshire (1981) The Geologic Investigation of the Taurus-Littrow Valley: Apollo 17 Landing Site. *Geological Survey Professional Paper,* 1080.
Wu, Y., Z. Wang, & Y. Lu (2019) Space weathering of the Moon from in situ detection. *Res. Astron. Astrophys. 19,* 051.
Yoder, H. S. (1976) Generation of Basaltic Magma. National Academy of Sciences, Washington, D.C.
Zhang, Y. & A. Zindler (1993) Distribution and evolution of carbon and nitrogen in Earth. *Earth & Planetary Science Letters. 117*, p. 331–345.
Zhang, L., X. Guo, Q. Wang, J. Ding, & H. Ni (2017) Diffusion of hydrous species in model basaltic melt. *Geochimica et Cosmchimica Acta, 215*, p. 377-386.
Zhang, L., X. Gao, W. Li, D. Zhou, L. Zhang, & H. Ni (2019) Reassessment of

pre-eruptive water content of lunar volcanic glass based on new data of water diffusivity. *Earth and Planetary Science Letters, 522,* p. 40-47.

Zimanowski, B., R. Buttner, V. Lorenz, & H-G. Hafele (1997) Fragmentation of basaltic melt in the course of explosive volcanism. *Journal of Geophysical Research, 102,* B1, p. 803-814.

VITA

Erin “Micki” Recchuiti received her Bachelor of Science degrees with honors in geology and anthropology with a minor in Japanese in Spring 2020 from Western Carolina University. While at Western Carolina University, she studied a variety of research topics including Inuit facial tattooing variations as seen in the archeological record, lunar meteorite geochemistry, paleocommunity dynamics in late Pennsylvanian marine invertebrates, and soil characteristics as an influence of soil creep in the Southern Appalachians. Her research was presented at several conferences as an undergraduate, such as the Southeastern Geological Society of America meetings in Knoxville, TN and Charleston, SC. After Western Carolina University, Micki began a Master of Science degree in geology at University of Tennessee Knoxville’s department of Earth and Planetary Sciences. Her advisor, Dr. Molly McCanta, supervised her studies on terrestrial and lunar volcanic glasses volatile content elucidated via geochemistry and spectroscopy. Micki was awarded the C. H. Gordon Award for Professional Promise by the Department of Earth and Planetary Sciences after her first year at the University of Tennessee Knoxville and had the opportunity to collaborate with researchers from Argonne National Laboratory and NASA’s Johnson Space Center’s Apollo Next Generation Sample Analysis program. The progress of her thesis work was presented at the American Geophysical Union 2020 conference and both the 2021 and 2022 Lunar and Planetary Science conferences.